

Ergodicity Breaking Under Confinement in Cold-Atom Quantum Simulators

Jean-Yves Desaulles¹, Guo-Xian Su^{2,3,4}, Ian P. McCulloch⁵,
Bing Yang⁶, Zlatko Papić¹, and Jad C. Halimeh^{7,8,*}

¹*School of Physics and Astronomy, University of Leeds, Leeds LS2 9JT, UK*

²*Hefei National Laboratory for Physical Sciences at Microscale and Department of Modern Physics, University of Science and Technology of China, Hefei, Anhui 230026, China*

³*Physikalisches Institut, Ruprecht-Karls-Universität Heidelberg, Im Neuenheimer Feld 226, 69120 Heidelberg, Germany*

⁴*CAS Center for Excellence and Synergetic Innovation Center in Quantum Information and Quantum Physics, University of Science and Technology of China, Hefei, Anhui 230026, China*

⁵*School of Mathematics and Physics, The University of Queensland, St. Lucia, QLD 4072, Australia*

⁶*Department of Physics, Southern University of Science and Technology, Shenzhen 518055, China*

⁷*Department of Physics and Arnold Sommerfeld Center for Theoretical Physics (ASC),*

Ludwig-Maximilians-Universität München, Theresienstraße 37, D-80333 München, Germany

⁸*Munich Center for Quantum Science and Technology (MCQST), Schellingstraße 4, D-80799 München, Germany*

(Dated: January 20, 2023)

The quantum simulation of gauge theories on synthetic quantum matter devices has gained a lot of traction in the last decade, making possible the observation of a range of exotic quantum many-body phenomena. In this work, we consider the spin-1/2 quantum link formulation of 1 + 1D quantum electrodynamics with a topological θ -angle, which can be used to tune a confinement-deconfinement transition. Exactly mapping this system onto a PXP model with mass and staggered magnetization terms, we show an intriguing interplay between confinement and the ergodicity-breaking paradigms of quantum many-body scarring and Hilbert-space fragmentation. We map out the rich dynamical phase diagram of this model, finding an ergodic phase at small values of the mass μ and confining potential χ , an emergent integrable phase for large μ , and a fragmented phase for large values of both parameters. We also show that the latter hosts resonances that lead to a vast array of effective models. We propose experimental probes of our findings, which can be directly accessed in current cold-atom setups.

I. INTRODUCTION

Gauge theories are quantum many-body models possessing gauge symmetries that dictate an intrinsic local relationship between matter and gauge fields [1–3]. The quantum simulation of gauge theories has progressed tremendously in recent years across various platforms of synthetic quantum matter [4–17]. This offers the opportunity to probe high-energy physics on low-energy tabletop platforms [18–25], establishing a valuable venue complementary to dedicated high-energy experiments, such as the Large Hadron Collider, and to classical computational methods, such as Quantum Monte Carlo. As an example, a cold-atom quantum simulator has recently been successfully employed in probing gauge invariance and thermalization dynamics in a U(1) gauge theory [13, 14], with concrete proposals [26, 27] of extending it to observe the confinement-deconfinement transition [28, 29]. In particular, Ref. [26] introduced a scheme that allows the realization of a tunable topological θ -angle term, which emerges in quantum electrodynamics [30–32] on account of the topological structure of the vacuum, and has profound consequences on quantum phases, dynamical behavior, and inherent symmetries. Tuning this angle can lead to confinement, an extremely active topic of research

in gauge theories [17, 33], and thus a tunable topological θ -angle term in a quantum simulator can allow the calculation of the time evolution of confined dynamics from first principles.

The understanding of ergodicity-breaking mechanisms in gauge theories sheds light on dynamics from high-energy particle physics to condensed matter physics and to the evolution of the early universe. Gauge-theory quantum simulators offer the prospect of probing ergodicity-breaking phenomena that are relevant to condensed matter physics, such as disorder-free localization [35–48], quantum many-body scars (QMBS) [6, 29, 49, 50], and Hilbert-space fragmentation (HSF) [51, 52], the understanding of which can provide a deeper generic picture of far-from-equilibrium dynamics in closed quantum many-body systems [53–55]. QMBS, a paradigm of weak ergodicity breaking, comprise states of anomalously low bipartite entanglement entropy that are usually equally spaced in energy across the entire spectrum of the Hamiltonian. Preparing a system in their subspace and quenching it will lead to persistent oscillations in local observables, an anomalously slow growth of bipartite entanglement entropy, and a corresponding significant delay in thermalization beyond any relevant timescales [6, 29, 49, 50]. Indeed, Bernien *et al.* [6] was the first experiment that observed QMBS in Rydberg arrays, and Surace *et al.* [29] were able to show that the implemented quantum Ising-like model maps onto the spin-1/2 U(1)

* jad.halimeh@physik.lmu.de

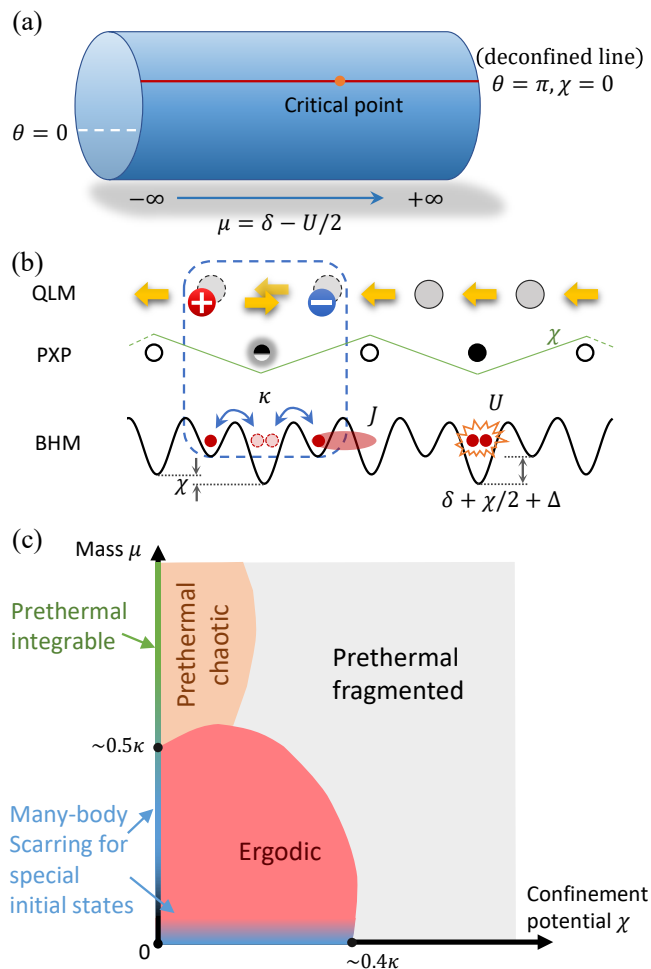


FIG. 1. (Color online). Tuning the topological θ -angle in the Bose–Hubbard quantum simulator. (a) The $U(1)$ quantum link model Hamiltonian (1) involves a topological θ -angle, where charges are deconfined at $\theta=\pi$, and Coleman’s phase transition occurs at effective mass $\mu=0.3275\kappa$, which corresponds to the spontaneous breaking of a global \mathbb{Z}_2 symmetry [34] that arises from the invariance of Hamiltonian (1) to transformations of parity and charge conjugation. (b) The staggered Bose–Hubbard model realizes the $U(1)$ quantum link model with direct tunneling J , on-site interaction U , staggered potential δ , and a small linear tilting potential Δ . By further adding a period-4 potential χ , the system is tuned away from $\theta=\pi$, leading to confinement. The $U(1)$ quantum link model or equivalently the staggered Bose–Hubbard model can be further mapped onto the PXP model where spins reside on the gauge links, and doublons on the gauge links represent spin excitations. (c) Schematic representation of the rich phase diagram in terms of confinement potential χ and effective mass μ . Fragmentation happens around $\chi \approx 0.4\kappa$.

quantum link model, which is a regularization of the lattice Schwinger model where the infinite-dimensional gauge fields of the latter are represented by spin-1/2 operators [56–58]. More recently, it has been shown that QMBS are ubiquitous in gauge theories, occurring over an extensive set of initial states [59, 60], in 2+1D [61],

and for spin- S representations of the gauge field when the system is prepared in highly excited vacua [62, 63]. This opens the question as to the gauge-theoretic origin of QMBS, which motivates exploring them further and extending their regimes in realistic gauge-theory quantum simulators.

On the other hand, HSF is a mechanism of ergodicity breaking emerging in models where the Hilbert space is fragmented into exponentially many invariant subspaces due to a exponentially large commutant algebra [51, 52, 64]. In the seminal case of dipole-conserving models [51, 52], HSF can be completely characterized by nonlocal integrals of motion [65]. More recently, HSF has also been shown to emerge in models with strict confinement [66, 67], including in gauge theories [68]. Experimental investigations of HSF have been carried out [69, 70], but exploring its presence in experimentally relevant parameter regimes of gauge theories would be very appealing, given recent large-scale cold-atom realizations of spin-1/2 $U(1)$ quantum link models [13, 14]. In this vein, one wonders whether QMBS can occur in regimes of confinement in gauge theories where HSF also arises, or whether scars are a purely deconfined phenomenon. Indeed while Ref. [29] showed a slowing of the dynamics under confinement, and Ref. [68] showed the emergence of a symmetry in the limit of strong confinement at zero mass, a full analysis of the fate of scarring with both mass and confining potential at intermediate values of experimental interest is lacking.

In this work, we explore the regime of finite mass and confining potential using exact diagonalization and matrix product state (MPS) techniques [71, 72]. We find prominent scarring regimes concomitantly with confinement, which we explain analytically and demonstrate numerically. We further map out the rich dynamical phase diagram where we find an ergodic phase for small values of the mass and confining potential. For larger values of these parameter, emergent conserved quantities at intermediate times appear, displaying a wide range of prethermal regimes with an emergent integrable phase for large mass in the deconfined regime, in addition to a fragmented phase for large values of both the mass and the confining potential,¹ as sketched in Fig. 1.

Our findings are based on the study of the PXP model, which exactly corresponds to the spin-1/2 $U(1)$ quantum link model (QLM) [29]. The latter has been demonstrated experimentally on a Bose–Hubbard quantum simulator [14]. The mapping between the different models is sketched on Fig. 1(b) and explained in details in Sec. II. Further, we demonstrate the experimental implementation of our findings numerically.

¹ We note that the emergent conserved quantities are only truly conserved for infinite values of μ/κ and χ/κ . For smaller values of these parameters the timescale it takes to propagate between Hilbert space fragments can already be too long to probe in experiment. We append the prefix “prethermal” to reflect this.

The rest of this paper is organized as follows: In Sec. II, we present the U(1) quantum link model with a topological θ -term and discuss its exact mapping onto the PXP model with a mass and staggered magnetization terms. In Secs. III and IV, we provide our analysis of scarring and fragmented dynamics, respectively, in the presence of confinement. In Sec. V, we discuss experimental probes in a state-of-the-art tilted Bose–Hubbard optical lattice that can facilitate the observation of our findings. We conclude and provide outlook in Sec. VI. Several Appendices and the Supplemental Material (SM) [73] contain supporting analytic and numerical results.

II. MODELS AND MAPPING

We now discuss the main models considered in this work, and briefly outline the mappings between them. For further details, the reader is referred to Refs. [26, 29].

A. U(1) quantum link model

The Schwinger model, which is 1 + 1D quantum electrodynamics, can be conveniently represented through the quantum link formulation, where the gauge and electric fields are represented by spin- S matrices [56–58], thereby facilitating experimental feasibility. Upon restricting to $S = 1/2$, and employing a Jordan-Wigner transformation to map the fermions onto Pauli operators and a particle-hole transformation on both the matter and gauge (electric) fields [26, 74], the resulting U(1) quantum link model (QLM) Hamiltonian takes the form

$$\hat{H}_{\text{QLM}} = \sum_{\ell=1}^{L_m} \left[-\frac{\kappa}{2} (\hat{\sigma}_{\ell}^{-} \hat{s}_{\ell, \ell+1}^{+} \hat{\sigma}_{\ell+1}^{-} + \text{H.c.}) + \frac{\mu}{2} \hat{\sigma}_{\ell}^{z} - \chi (-1)^{\ell} \hat{s}_{\ell, \ell+1}^{z} \right], \quad (1)$$

where now the Pauli operator $\hat{\sigma}_{\ell}^z$ represents the matter field on site ℓ , and the spin-1/2 operator $\hat{s}_{\ell, \ell+1}^{+(z)}$ represents the gauge (electric) field at the link between sites ℓ and $\ell + 1$. We consider a lattice with L_m sites and L_m links under periodic boundary conditions (PBC). The deviation from the deconfined point $\theta = \pi$ is quantified by the *confining potential* $\chi = g^2(\theta - \pi)/(2\pi)$ [26]. At $\chi = 0$, the U(1) QLM undergoes a second-order quantum (Coleman) phase transition at $\mu/\kappa = 0.3275$ related to the spontaneous breaking of a global \mathbb{Z}_2 symmetry arising due to the invariance of Eq. (1) under a parity and charge (CP) transformation at $\chi = 0$ [34, 75, 76]. When $\chi \neq 0$, the global \mathbb{Z}_2 symmetry is explicitly broken by the last term in Eq. (1), and the Coleman phase transition is no longer present. The generator of the U(1) gauge symmetry of Hamiltonian (1) is

$$\hat{G}_{\ell} = (-1)^{\ell} \left(\hat{s}_{\ell, \ell+1}^{z} + \hat{s}_{\ell-1, \ell}^{z} + \frac{\hat{\sigma}_{\ell}^{z} + \hat{\mathbb{1}}}{2} \right), \quad (2)$$

which can be construed as a discretized version of Gauss’s law. Throughout this work, we will work in the physical sector of Gauss’s law, defined by the set of gauge-invariant states $\{|\psi\rangle\}$ satisfying $\hat{G}_{\ell}|\psi\rangle = 0, \forall \ell$.

Despite being a regularization of the Schwinger model, the U(1) QLM (1) still captures a wealth of the physics of the Schwinger model, including Coleman’s phase transitions at $\chi = 0$ [34], and the confinement-deconfinement transition [77].

B. PXP Hamiltonian

The U(1) QLM with a topological θ -term, described by Hamiltonian (1), can be mapped onto the PXP model with a staggered-magnetization term [29, 62, 63], described by the Hamiltonian

$$\begin{aligned} \hat{H}_{\text{PXP}} &= -\kappa \hat{\mathcal{P}} \left(\sum_{l=1}^{L_m} \hat{s}_l^x \right) \hat{\mathcal{P}} - \sum_{l=1}^{L_m} [2\mu + (-1)^l \chi] \hat{s}_l^z \\ &= -\kappa \sum_{l=1}^{L_m} \hat{P}_{l-1} \hat{s}_l^x \hat{P}_{l+1} - \sum_{l=1}^{L_m} [2\mu + (-1)^l \chi] \hat{s}_l^z, \quad (3) \end{aligned}$$

where we have assumed PBC, integrated out the degrees of freedom on the matter sites, and relabelled the gauge sites as $\hat{s}_{l, l+1}^{\alpha} \rightarrow \hat{s}_l^{\alpha}$ for notational brevity.² The projector $\hat{\mathcal{P}}$ annihilates any configuration with neighboring up-spins, in order to only allow configurations that respect Gauss’s law. The Hamiltonian also admits a local formulation using the on-site projector $\hat{P}_l = \frac{1}{2} - \hat{s}_l^z$ that annihilates any component with $s_l^z = +1/2$. This Hamiltonian corresponds to the PXP model with detuning μ and staggered detuning χ . For $\chi = 0$, the PXP model has been extensively studied in the context of QMBS both theoretically and experimentally [6, 29, 50, 59]. It has also been studied in the context of HSF in the limit of $\chi/\kappa \gg 1$ [68].

In the following sections, we will explore both the ergodic and fragmented regimes of the PXP model with a staggered magnetization term. The approximate values of μ and χ to which these correspond for $L_m \approx 30$ are schematically illustrated in Fig. 1, (see Appendix A for actual data).

III. QUANTUM MANY-BODY SCARRING IN THE PRESENCE OF CONFINEMENT

For simplicity, we shall set $\kappa = 1$ as the overall energy scale and focus on the PXP model (3) in this section. The PXP Hamiltonian has been known to host

² For open boundary conditions, Eqs. (1) and (3) can also be mapped onto each other, where the results of the latter are similar to those obtained for the U(1) QLM, but with μ and χ halved on the two boundary spins.

QMBS linked to the Néel state $|\bullet\bullet\dots\bullet\bullet\rangle$ and anti-Néel state $|\circ\circ\dots\circ\circ\rangle$ for $\mu = \chi = 0$ [6, 50]. Scarring was also observed experimentally from the polarized state $|\circ\circ\dots\circ\circ\rangle$ for $\mu \approx \pm 0.4$ [59]. Here, for historical purposes [6], a filled (empty) circle denotes a Rydberg atom in the excited (ground) state, but one can equivalently think of it as a spin-1/2 particle in the up (down) eigenstate. The Néel and anti-Néel states correspond to the two vacua of the PXP model, i.e., its degenerate ground states at $\mu \rightarrow \infty$, while the polarized state corresponds to the charge-proliferated state, which is the nondegenerate ground state of the PXP model at $\mu \rightarrow -\infty$. These two realizations of QMBS occur in the ergodic regime in Fig. 1(c). This means that other initial states display the expected thermalizing behavior and other probes of chaos such as level spacing statistics are those of a chaotic system. In this section, we focus on this region and discuss the impact of confinement on QMBS. One would generally expect it to strongly modify the dynamics and lead to the disappearance of revivals from scarred initial states. While this indeed happens for the polarized state at intermediate values of χ , we will show that this is not true for the Néel state, where the confining term actually *enhances* scarring.

In order to assess the effect of the confining potential, we compute the self-fidelity $\mathcal{F}(t) = |\langle \psi_0 | e^{-i\hat{H}_{\text{PXP}}t} | \psi_0 \rangle|^2$, where $|\psi_0\rangle$ is the initial state of the system. We will denote the first peak of the self-fidelity by \mathcal{F}_1 , and the self-fidelity at half that time by $\mathcal{F}_{1/2}$. As QMBS are characterized by the wave function spreading into the Hilbert space before refocusing close to the initial state, their signature is $\mathcal{F}_1 \approx 1$ and $\mathcal{F}_{1/2} \approx 0$. Hence, we will use the quantity $\mathcal{F}_1 - \mathcal{F}_{1/2}$ as a probe of QMBS. This quantity distinguishes QMBS from the trivial situation where the initial state is close to an eigenstate, in which case $\mathcal{F}(t) \approx 1$ at all times.

We show $\mathcal{F}_1(t)$ and $\mathcal{F}_1(t) - \mathcal{F}_{1/2}(t)$ for the PXP model with $\mu = 0$ and staggered magnetization in Fig. 2(a), bottom panel, starting in the Néel state. We find interesting nonmonotonic behavior as a function of χ in these quantities that we further analyze in the following. The effect of the staggered magnetization on its own in the PXP model has been studied in Ref. [68] in the limit of $\chi \gg \kappa$. In this regime, the Hilbert space fractures and an emergent symmetry appears due to an approximate $\text{su}(2)$ algebra. The same inexact spectrum-generating algebra has been linked to quantum many-body scars in the PXP model [78–80]. In that algebraic picture, the PXP Hamiltonian can be thought of as the global \hat{J}^x operator, leading to a dynamics that resembles the precession of a large spin when initialized in the Néel state. This state is in fact the highest-weight state of the effective global \hat{J}^z operator, hence why it would have perfect revivals when acted upon by \hat{J}^x if the algebra was exact. It has recently been proposed that the origin of this approximate algebra is a parent spin-1 Hamiltonian [81]. When $\mu = 0$, the PXP Hamiltonian can be obtained by projecting the global spin operators from the parent model onto

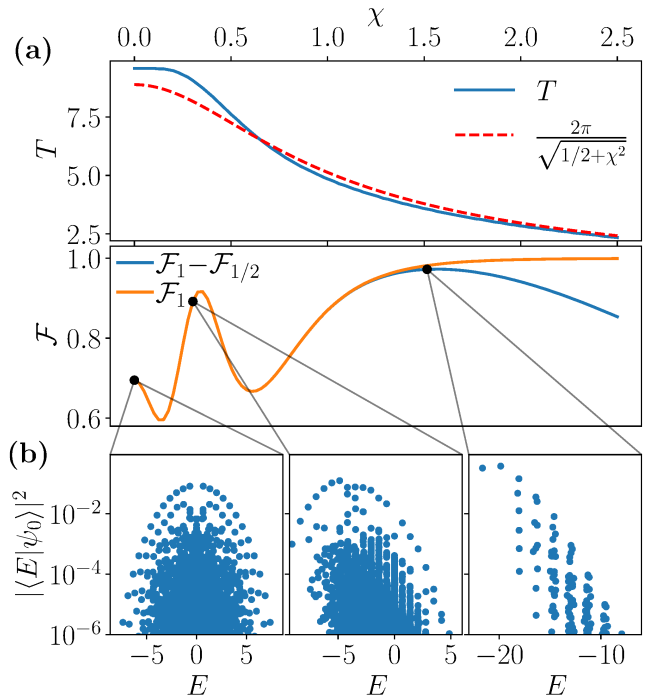


FIG. 2. (Color online.) (a) Revival amplitude and period from the Néel state for the PXP model with staggered detuning and $N = 26$. For all values of χ we see a high value of \mathcal{F}_1 indicating high revivals. However as χ becomes large the Néel state gets closer and closer from being an eigenstate, leading to an increase of $\mathcal{F}_{1/2}$ and so a decrease of $\mathcal{F}_1 - \mathcal{F}_{1/2}$. The nonmonotonicity of \mathcal{F} with χ is likely due to the interaction with lower band of eigenstates. (b) Overlap between the Néel state and the eigenstates for $\chi = 0$, $\chi = 0.3$ and $\chi = 1.52$. For the anti-Néel or for $\chi < 0$, the dynamics is exactly the same but the spectrum is flipped with respect to $E = 0$.

the constrained Hilbert space and applying the mapping $|-\rangle = |\uparrow\downarrow\rangle$, $|0\rangle = |\downarrow\downarrow\rangle$, and $|+\rangle = |\downarrow\uparrow\rangle$, where site j of the spin-1 model maps to sites $2j - 1$ and $2j$ of PXP³. As such, we can write

$$-\frac{1}{\sqrt{2}}\hat{P}\hat{S}^x\hat{P} - \chi\hat{P}\hat{S}^z\hat{P} = \hat{H}_{\text{PXP}} \oplus 0_{\perp}, \quad (4)$$

when $\mu = 0$ and $\kappa = 1$, where \hat{S}^{α} are the global spin operators in the spin-1 model and 0_{\perp} is the part of the spin-1 Hilbert space that is annihilated by the PXP constraint. Had the projection operator commuted with the spin operators, we would have had perfect revivals in the PXP model from the Néel state with a period

$$T = \frac{2\pi}{\sqrt{\chi^2 + \frac{1}{2}}}. \quad (5)$$

³ One can alternatively take a mapping where site j of the spin-1 model maps to sites $2j$ and $2j + 1$. In that case the results are the same except that the minus sign in front of the $\hat{P}\hat{S}^z\hat{P}$ term in Eq. 4 is replaced by a plus sign.

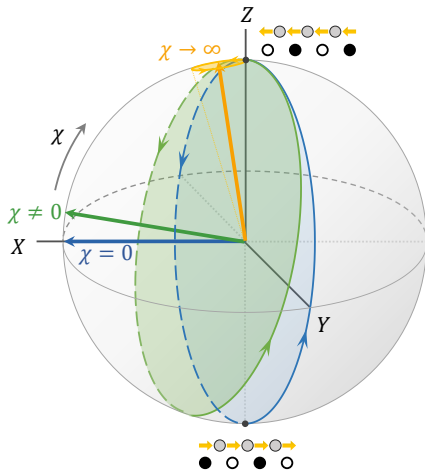


FIG. 3. (Color online). Schematic picture of the effect of the confining potential on the dynamics after a quench from the Néel (or vacuum) state. The X , Y and Z labels refer to the the approximate $\text{su}(2)$ algebra.

Figure 2(a), top panel, shows that while it is not exactly the case, we still obtain results that closely resemble this picture. The agreement also gets better as χ is increased. This is likely due to the fact that \hat{S}^z commutes with $\hat{\mathcal{P}}$ while \hat{S}^x does not.

As χ gets larger than roughly 1.5, we see that $\mathcal{F}_1 - \mathcal{F}_{1/2}$ starts to decrease as the minimum fidelity between the revivals increases. This can be understood easily in the spin-precession picture. Indeed, we can visualize this whole process on a Bloch sphere. The Néel state is at the top, along the Z axis. For $\chi = 0$, the precession axis is along the X axis, on the equator. As χ is increased, the precession axis is moved closer and closer to the Z axis. Hence, the “opposite point” of the trajectory is no longer the anti-Néel state, but another state placed on the opposite side of the precession axis. As χ is further increased, this opposite point gets closer and closer to the Néel state. In the limit of $\chi \rightarrow \infty$, the precession axis becomes the Z axis and the Néel state an exact eigenstate of the system. Figure 3 shows this schematically on a Bloch sphere. The effect of this “axis tilting” can also be seen directly in the overlap between the Néel state and the corresponding PXP eigenstates at various values of χ , as shown in Fig. 2(b). The top band of scarred states is always visible. However, as χ is increased, the eigenstates with the highest overlap shift from the middle of the spectrum to its left edge where the ground state is. Note that for the largest value of χ plotted the energy spectrum starts to split into bands. This will be addressed in Sec. IV.

While this precession picture predicts revivals at all values of χ and gives a good approximation of the period, it fails to capture the presence of the optimal revival point around $\chi = 0.35$; see Fig. 2(a). At that value,

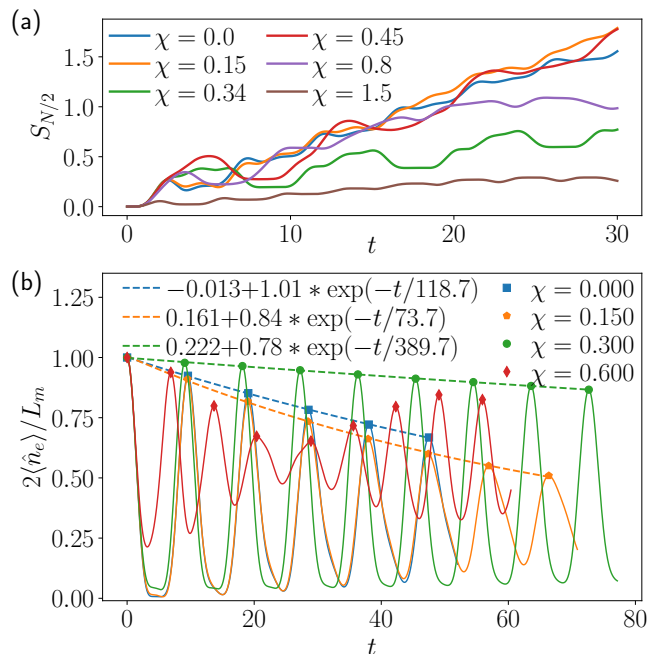


FIG. 4. (Color online). (a) Bipartite von Neumann entanglement entropy after a quench from the Néel state for $L_m = 26$ and various values of χ . The entropy growth is strongly suppressed around $\chi = 0.35$. (b) Excitation density on odd sites for $L_m = 32$ and various values of χ and their exponential fit. Only times for which the expectation values are converged in system size are used. Once $\chi \geq 0.5$ oscillations are visible in the peaks and an exponential decay no longer describes their behavior with time.

the Néel state is still far from the edges of the spectrum and the level statistics are also indicative of ergodicity (see Appendix A). The revivals at that point converge very quickly in system size and are not visible for other initial states, which generically thermalize relatively fast; see Supplemental Material (SM) [73].

Focusing on the Néel state, we find that the growth of entanglement entropy is also highly suppressed at $\chi = 0.35$, as shown in Fig. 4(a). This nonmonotonicity in the post-quench behavior relative to χ can be witnessed in local observables, making it measurable in a large-scale experiment. For a local observable, we choose the excitation density $\langle \hat{n}_o \rangle$ on the odd sublattice, as this should be easily measurable. In order to avoid finite-size effects, we also consider only the times where the dynamics is converged in system size for $L_m = 32$. As this observable is oscillating in time, we first identify the local maxima in order to fit its envelope. The details of this procedure are explained in the SM [73], and the results are shown in Fig. 4(b) for several values of χ . Overall, we find a clear difference between $\chi = 0.3$ and the other values already after three to four revivals. The decay time τ also shows a much larger value around $\chi = 0.3$ (see legend-equations). Finally, we see that for $\chi = 0.6$ the peaks themselves show an oscillatory behavior and

are no longer well approximated by a decaying exponential. We emphasize that this is not a finite-size effect but rather a sign that we enter the low-energy regime where only a handful of eigenstates contribute. The oscillation in the maxima is then a beating frequency linked to the mismatch in the energy spacing of these eigenstates.

The above results all show that setting $\chi \approx 0.35$ significantly enhances scarring compared to $\chi = 0$ when starting in the Néel state. This enhancement can be linked to a top band well separated from the bulk and with a more even energy spacing between states in it. This implies that at that point the approximate $\text{su}(2)$ structure is closer to exact than for other values of χ . This is shown in details in Appendix B, and further investigated using the forward scattering approximation (FSA) [50]. This method allows to build an approximate version of the $L_m + 1$ scarred eigenstates, thus removing any influence from the bulk of thermal states. Even in that case, the same nonmonotonic behavior in χ is seen. Its origin in this simplified picture can then be understood as stemming from two competing factors: (i) how well it can be approximated by a $L_m + 1$ level system, and (ii) how close the hopping strength are to that of a spin $L_m/2$. While the former is optimal at $\chi = 0$ and $\chi = \pm\infty$, for the latter it is at $\chi \approx \pm 0.42$ and $\chi = \pm\infty$. Due to these two competing factors, we find three local maxima in the fidelity at $\chi = 0$, $\chi \approx \pm 0.4$, and $\chi = \pm\infty$. While the exact value of the optimal point is not exactly the same in the FSA as in the full model (likely due to the further influence of the states outside of the top band), this approach provides an explanation to the nonmonotonic behaviour.

A. Defects and confinement

While adding a nonzero χ affects the algebra and the revivals from the Néel state, from a lattice gauge theory point of view it also causes confinement [26–29]. Notably, each particle-antiparticle pair has an energy cost $\propto d\chi$, where d is the distance between the particle and the antiparticle. For $\chi = 0$, this cost is zero and so they can spread ballistically in opposite directions, i.e., they are deconfined. As soon as $\chi > 0$, any separation distance is penalized, leading to their confinement.

In the picture of the PXP model, neighboring unexcited sites $|\circ\circ\rangle$ means the presence of a particle or antiparticle between them (depending if the sites are even-odd or odd-even). Similarly, an excited site next to an unexcited site ($|\circ\bullet\rangle$ or $|\bullet\circ\rangle$) means that there is no particle/antiparticle between them. So a single particle-antiparticle pair on top of the vacuum will take the form of a single “defect” on top of the Néel (or anti-Néel) state. More precisely, we will use the state $|\circ\bullet\bullet\cdots\circ\bullet\bullet\circ\bullet\cdots\circ\bullet\bullet\rangle$, which corresponds to the Néel state with an excitation removed on site M near the middle of the chain. This can also be understood as creating two domain-walls between Néel domains $\circ\bullet\bullet$ and

anti-Néel domains $\bullet\circ\circ$. We quench this state and monitor the excitation occupancy on each site $\langle\hat{n}_j\rangle$. We also monitor the presence of domain-walls using the quantity $\langle(1 - \hat{n}_j)(1 - \hat{n}_{j+1})\rangle = 1 - \langle\hat{n}_j\rangle - \langle\hat{n}_{j+1}\rangle$, where we have utilized that $\langle\hat{n}_j\hat{n}_{j+1}\rangle = 0$. Finally, we track the ZZ connected correlator $\langle\hat{s}_M^z\hat{s}_j^z\rangle_c = \langle\hat{s}_M^z\hat{s}_j^z\rangle - \langle\hat{s}_M^z\rangle\langle\hat{s}_j^z\rangle$. The corresponding results at $\chi = 0$ and $\chi = 0.35$ are shown in Fig. 5, which have been obtained by matrix product state (MPS) techniques with OBC in conformance with experimental relevance. MPS allows us to probe large system sizes where the boundary is not reached even at long times (more details about this can be found in SM [73]). The ZZ correlator shows a clear difference between the two values of χ used. Interestingly, for $\chi = 0.35$ at late times the effects of the defects are barely visible whereas for $\chi = 0$ they still are. The oscillations between the two domain walls (so the anti-Néel domain) seems to synchronize with the oscillation outside of the domain walls (the Néel domain). For $\chi = 0$ the two regions seem to oscillate at the same frequency but with a π phase difference. While it is not clear if this is linked to the enhancement of revivals without any defect, this kind of “self-correction” of defects is also experimentally desirable.

In order to quantify confinement more precisely, we compute the “root mean square spread” of the ZZ correlator as

$$\sigma(|zz\rangle) = \sqrt{\frac{\sum_{j=1}^{L_m} |\langle\hat{s}_j^z\hat{s}_M^z\rangle|(j-M)^2}{\sum_{j=1}^{L_m} |\langle\hat{s}_j^z\hat{s}_M^z\rangle|}}. \quad (6)$$

We plot this quantity at all times for $\chi = 0$ and $\chi = 0.35$ in Fig. 6. There, we can see a clear difference between the two, as for $\chi = 0.35$ the spreading plateaus around $t \approx 30$ while for $\chi = 0$ it continues at later times until it reaches the boundary.

IV. HILBERT SPACE FRAGMENTATION INDUCED BY CONFINEMENT

The mass term in Eq. (3) does not fit into the approximate algebra discussed above, and it generically destroys revivals from the Néel state, thereby destroying scarring from this state. However the combination of nonzero mass and confining potential allows a more complex picture to emerge due to the interplay between these two terms.

In the regime $\chi, \mu \gg \kappa$, one can perform a Schrieffer-Wolff transformation. For general values of μ and χ , one can use a procedure such as in Ref. [68], which studies the case with $\mu = 0$. We show the main results in this section, while all details are relegated to the SM [73]. We find that the odd-order terms are identically zero. The leading term is then the second-order one, which is diagonal and reads

$$\hat{H}_{\text{eff}}^{(2)} = -\frac{\kappa^2}{2} \sum_{j=1}^{L_m} \frac{\hat{P}_{j-1}\hat{s}_j^z\hat{P}_{j+1}}{2\mu + (-1)^j\chi}. \quad (7)$$

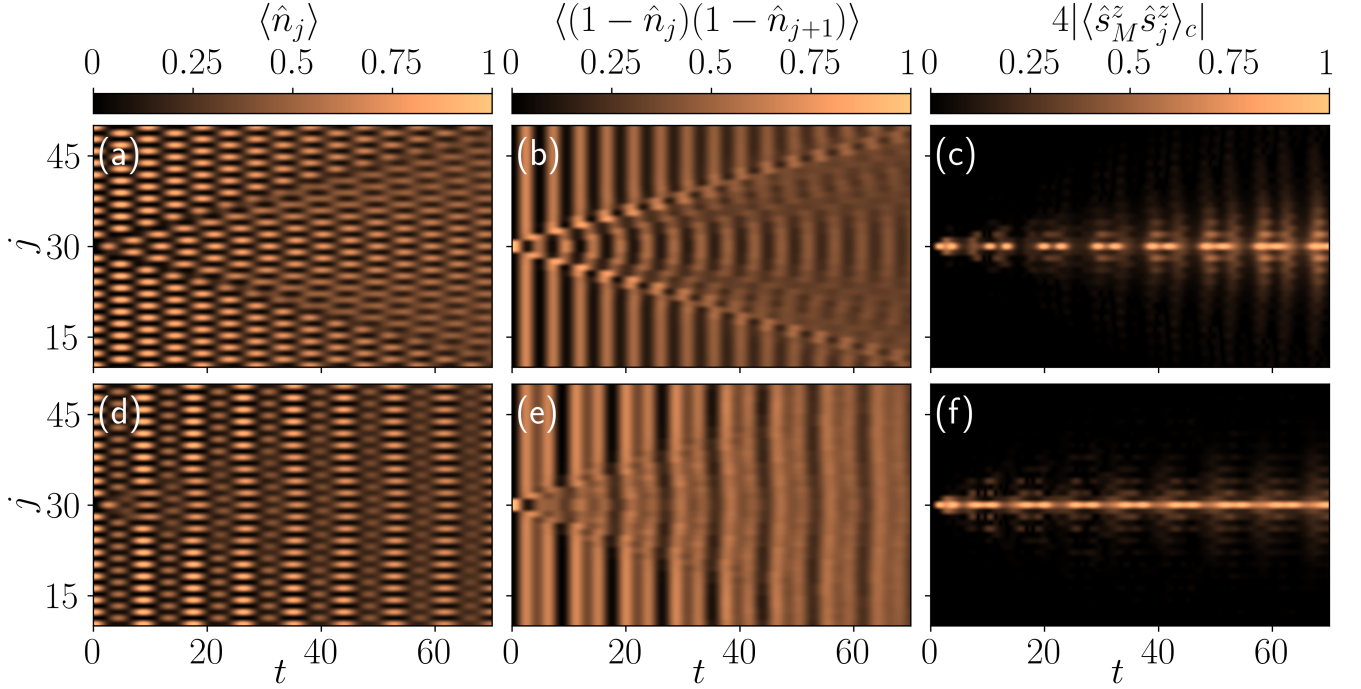


FIG. 5. (Color online). Observable dynamics after a quench from the Néel state with a defect with $L_m = 61$ and OBC. The data is truncated to only focus on sites near the middle of the chain where the defect was initially localized. (a)-(c) $\chi = 0$ (d)-(f) $\chi = 0.35$. The effect of confinement is visible for the ZZ correlator in panels (c) and (f). At late times, the Néel and anti-Néel domains are still clearly distinguishable in panels (a) and (b) but not in panels (c) and (d).

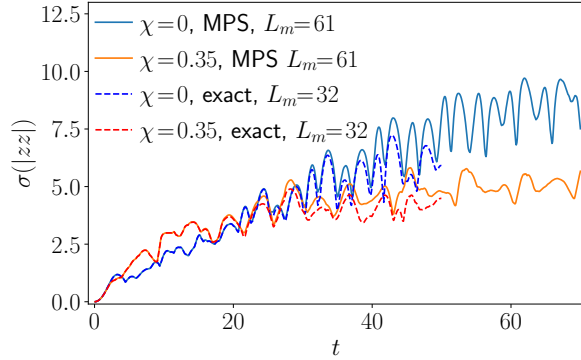


FIG. 6. (Color online). Root mean square of the spread of the connected correlator between Pauli Z matrices at the middle site and other sites. The exact and MPS data coincide well at shorter times, when the influence of the chain boundaries are small. In both cases, the confinement induced by χ is clear.

As this term is diagonal, we need to go to the next nonzero order for dynamics to occur in the Z basis. This happens at fourth order with an effective Hamiltonian

given by

$$\begin{aligned} \hat{H}_{\text{eff}}^{(4)} = & \frac{\kappa^4}{32} \sum_{j=1}^{L_m} 4 \frac{\hat{P}_{j-1} \hat{s}_j^z \hat{P}_{j+1}}{(2\mu + (-1)^j \chi)^3} \\ & + 2 \frac{4\mu - (-1)^j \chi}{(4\mu^2 - \chi^2)^2} \left(\hat{P}_{j-2} \hat{P}_{j-1} \hat{s}_j^z \hat{P}_{j+1} + \hat{P}_{j-1} \hat{s}_j^z \hat{P}_{j+1} \hat{P}_{j+2} \right) \\ & + \frac{4\mu + (-1)^j \chi}{(4\mu^2 - \chi^2)^2} \left(\hat{P}_{j-2} \hat{s}_j^+ \hat{P}_j \hat{s}_{j+1}^- \hat{P}_{j+2} + \text{H.c.} \right). \end{aligned} \quad (8)$$

We obtain a similar expression as in Ref. [68], with a purely diagonal term at second order. This is despite the addition of the mass term that “breaks” the approximate $\text{su}(2)$ algebra. This is because additional terms due to a nonzero μ are nonresonant at low order except in the special case of $\mu = 0$. So in general, additional terms due to a nonzero μ will generally appear only at higher order when away from resonances.

A. $\chi = \pm 2\mu$ Resonance

One clear feature of both Hamiltonians (7) and (8) is that some of their terms diverge if $\chi = \pm 2\mu$ due to a resonance condition. Let us focus on the case $\chi = -2\mu$. Then we have that $2\mu + (-1)^j \chi = 2\mu [1 - (-1)^j]$ is equal to 4μ for odd j and to 0 for even j . So only spin-flips on odd sites lead to an energy change. In the limit $\chi, \mu \gg \kappa$,

then the odd sites are effectively frozen as the energy cost to change them is too high. Hence, the Hilbert space fractures into $2^{L_m/2}$ sectors corresponding to all the possible combinations of the spins on odd sites. The sites that are frozen in the excited position also freeze their neighboring sites due to the PXP constraint. The remaining spins on even sites that have no up-spin neighbors can be excited freely and independently, and thus the effective model at leading order is that of a free spin-1/2 paramagnet.

We can extend our analysis to other values of μ and χ around the resonance such that $\chi = -2\mu + \gamma$ and $\mu, \chi \gg \kappa, \gamma$. The leading Schrieffer-Wolff term is at first order and reads

$$\hat{H}_{\text{eff}}^{(1)} = -\kappa \sum_{j \in \mathcal{K}} \hat{s}_j^x - \sum_{j=0}^M \gamma \hat{s}_{2j}^z = E_0 - \sum_{j \in \mathcal{K}} (\kappa \hat{s}_j^x + \gamma \hat{s}_j^z), \quad (9)$$

where \mathcal{K} is the set of all even sites with both neighbors frozen in the down position and E_0 is the (constant) contribution of all frozen even sites (so with at least one neighbour in the up position). This Hamiltonian is then clearly integrable for all values of κ and γ .

We show the effects of this resonance in quenching from the Néel and polarized states in Fig. 7. While this fragmentation affects all initial states unlike QMBS, we only show these two initial states for brevity and as they are the most relevant one for experimental preparation. For both of them, strong revivals of the wavefunction can be seen around the resonance already as relatively small values of χ and μ . For the Néel state, only $\chi = -2\mu$ leads to revival and not $\chi = 2\mu$. Indeed, in the latter case this state is completely frozen as you cannot deexcite even sites, which in turn prevent the odd ones to be excited.

For the polarized state the pattern is more complicated. This might seem surprising as this state is in the same Hilbert space sector as the Néel state. However, the terms in the Hamiltonian connecting the sectors (changing the state of off sites) are much less suppressed for the polarized state than for the Néel state, as for the latter two even sites must first be de-excited before such a move can be done. Hence even for large values of μ the odd sites cannot be considered as totally frozen and we have some weak couplings between the Hilbert space sectors. This leads to further restriction for revivals in order to make all sectors aligned in energy, as shown on Fig. 8. The additional resonance condition can be cast as

$$\chi = \frac{n\sqrt{1+\gamma^2}}{2}, \quad \mu = \frac{\gamma - \chi}{2} \quad (10)$$

with n an integer (see Appendix C for details). The case $\gamma = 0$ yields the condition for χ to be half-integer or integer. Alternatively, we can get rid of γ and write the relation between μ and χ directly as

$$\frac{(2\chi)^2}{n^2} - (2\mu + \chi)^2 = 1. \quad (11)$$

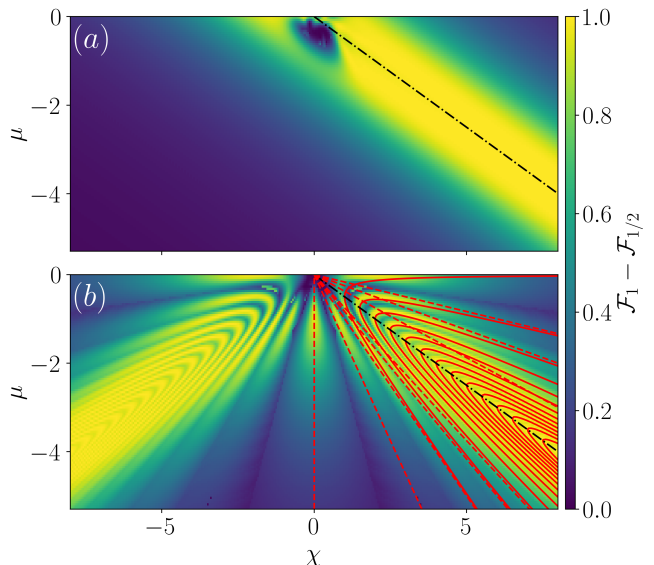


FIG. 7. (Color online). Self-fidelity from (a) the Néel state and (b) polarized state in the PXP model with $L_m = 20$. The black dash-dotted line shows the resonance line $\chi = -2\mu$, while the red hyperbolas show the optimal revival around it. The red dashed lines show the other resonances $\mu = -\frac{n+1}{n-1}\chi$.

We recognize here the equation for a hyperbola, and it is shown on Fig. 7(b) for various values of n . Fig. 8 illustrates how all eigenstates are approximately equally spaced as long as these equations are followed.

B. Other resonances

Beyond $\chi = \pm 2\mu$, there are other resonant ratios between μ and χ . Exciting an even site leads to a change in energy of $\Delta E_1 = -2\mu - \chi$ while on an odd site it costs $\Delta E_2 = -2\mu + \chi$. In order to have resonances, we want ΔE_1 and ΔE_2 to be commensurate. The two simplest cases are if ΔE_1 is an integer multiple of ΔE_2 or vice versa. This leads to the resonance condition

$$\mu = \pm \frac{n+1}{2(n-1)}\chi, \quad (12)$$

with n an integer (which can also be negative or equal to 0). These lines are plotted in red and dashed on Fig. 7(b). The only notable ones that lead to changes in the effective Hamiltonian at order 4 or below, are $\chi = 0$ and $\mu = \frac{3}{2}\chi$. Note that unlike the resonance at $\chi = \pm 2\mu$, in these two cases we do not expect to see revivals on Fig. 7 at large values of χ and μ , as the polarized and Néel states become eigenstates. Nonetheless, revivals can be seen at intermediate values along these resonances for the polarized state.

The effective Hamiltonian around $\chi = 0$ also leads to interesting properties. If $\mu \gg \chi$, the total number of excitations becomes conserved. The effective Hamiltonian at second order then gains a nearest-neighbor XY

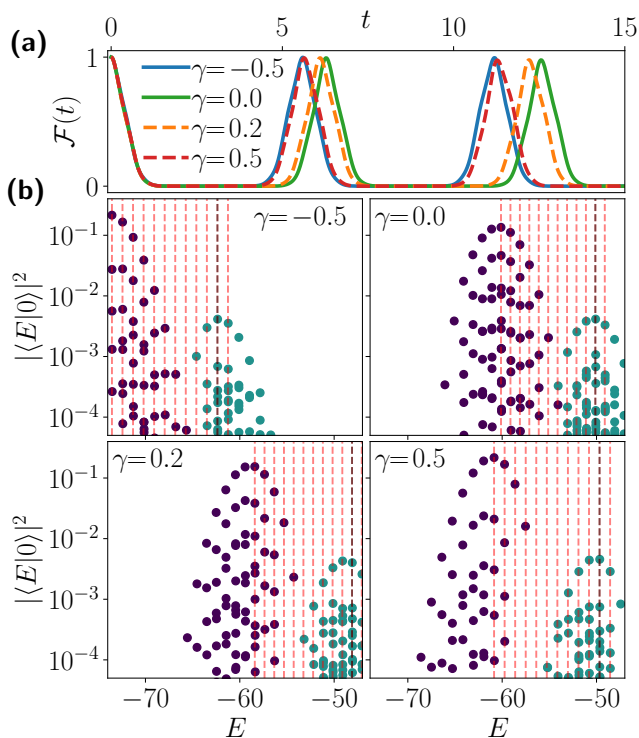


FIG. 8. (Color online). Quenches from the polarized state in the PXP model with $L_m = 24$ around the resonance line as $\chi = 5\sqrt{1+\gamma^2}$ and $\mu = \frac{\gamma-\chi}{2}$. (a) Self-fidelity after a quench. As γ is varied the period changes but the revivals remain close to perfect. (b) Overlap between polarized state and the eigenstates. The color indicates the occupation density of the odd sites, and as the various sectors. The red dashed lines are all spaced in energy by $\sqrt{1+\gamma^2}$, while the grey dashed line is placed with energy difference 2χ from the highest overlap eigenstate. In all cases of γ we see that all eigenstates show close to equal spacing.

type term, and a small χ will add some additional diagonal term at first order. The effective Hamiltonian then becomes

$$\hat{H}_{\text{eff}}^{(1,2)} = -\frac{\kappa^2}{8\mu} \sum_{j=1}^{L_m} \left(2\hat{P}_{j-1} \hat{s}_j^z \hat{P}_{j+1} + \hat{P}_{j-1} \hat{\sigma}_j^+ \hat{\sigma}_{j+1}^- \hat{P}_{j+2} + \text{H.c.} \right) - \sum_{j=1}^{L_m} (-1)^j \chi \hat{s}_j^z. \quad (13)$$

There is no fragmentation for that Hamiltonian, as each U(1) sector is fully connected. But what is interesting to note, is that for $\chi = 0$ this effective Hamiltonian resembles the lattice fermions \mathcal{M}_1 supersymmetric model introduced in Ref. [82]. The two terms that compose the Hamiltonian are the same, but their prefactors are different. Nonetheless, the same mapping to the an XXZ-type model can be done, albeit with a different value of Δ . Consequently, in each of the U(1) sectors the effective Hamiltonian is integrable. However, as soon as $\chi \neq 0$, this Hamiltonian no longer maps to an XXZ-type model,

and when χ and $\frac{\kappa^2}{8\mu}$ are of comparable strength we find level spacing statistics close to Wigner-Dyson (see Appendix A).

Overall, the interplay of the mass and confining terms allows for a vast array of regimes. It should be noted that while our Schrieffer-Wolff transformations are performed assuming that μ or χ are much larger than κ , we observe the onset of fragmentation already for relatively small values of these parameters such as $\mu = 0$, $\chi = \kappa/2$ for $L_m = 28$. This can be seen in the dynamics and even in the energy levels statistics (see Appendix A). Nonetheless, this is likely a finite-size effect as larger values of χ and μ are needed to escape the ergodic region as L_m is increased.

V. EXPERIMENTAL PROBES IN A BOSE-HUBBARD SIMULATOR

The U(1) QLM has been experimentally implemented on a Bose-Hubbard quantum simulator for the deconfined case of $\chi = 0$, where gauge invariance was directly observed [13], and thermalization dynamics was probed [14]. More recently, an experimental proposal outlines how these experiments can be feasibly updated to study confinement in this model [26, 27]. The Hamiltonian of this tilted Bose-Hubbard model employed in these works is

$$\hat{H}_{\text{BHM}} = -J \sum_{j=1}^{L-1} (\hat{b}_j^\dagger \hat{b}_{j+1} + \text{H.c.}) + \frac{U}{2} \sum_{j=1}^L \hat{n}_j (\hat{n}_j - 1) + \sum_{j=1}^L \left[(-1)^j \frac{\delta}{2} + j\Delta + \frac{\chi_j}{2} \right] \hat{n}_j, \quad (14)$$

where J is the tunneling strength, U is the on-site interaction strength, \hat{b}_j and \hat{b}_j^\dagger are bosonic ladder operators satisfying the canonical commutation relations $[\hat{b}_j, \hat{b}_r^\dagger] = \delta_{j,r}$, $\hat{n}_j = \hat{b}_j^\dagger \hat{b}_j$ is the bosonic number operator at site j , and Δ is an overall tilt. The staggering potential δ distinguishes between matter sites (even j) and gauge links (odd j). Connecting this to Eq. (1) means that ℓ corresponds to even bosonic sites j , while the link between ℓ and $\ell+1$ corresponds to odd bosonic sites j , where the bosonic model (14) hosts a total of $L=2L_m$ sites, with L_m the number of matter sites. The second staggering potential,

$$\chi_j = \begin{cases} 0 & \text{if } j \bmod 2 = 0, \\ \chi & \text{if } j \bmod 4 = 1, \\ -\chi & \text{if } j \bmod 4 = 3, \end{cases} \quad (15)$$

is related to the topological θ -term, and in the bosonic lattice distinguishes between odd and even gauge links, but has no effect on the matter sites.

The mapping between the bosonic and QLM representations is such that on an even bosonic site, which represents a site of the QLM, the presence of a single boson represents matter occupation, while no bosons means

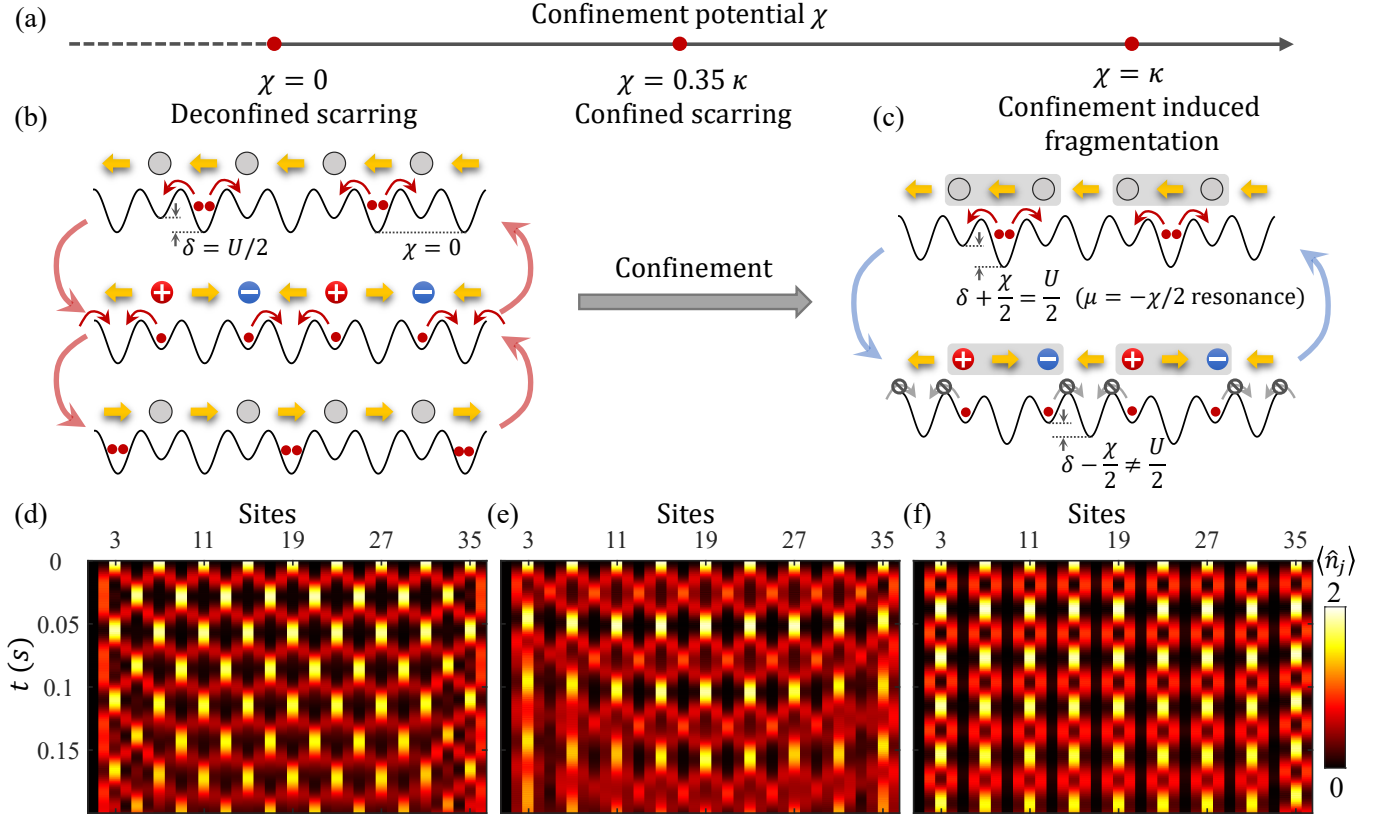


FIG. 9. (Color online) Proposed experimental realization of the confinement-induced scarring and fragmentation in a Bose-Hubbard quantum simulator. (a) By tuning confinement potential χ from 0, regimes of the deconfined scarring ($\chi = 0$), confinement-enhanced scarring ($\chi = 0.35\kappa$), and confinement-induced fragmentation (using the resonant case $\chi = \kappa$, $\mu = -0.5\kappa$ as an example) can be realized. (b) and (d): Schematic and MPS simulation of the deconfined scarring, the “state transfer” between the two vacuums. (c) and (f): In the fragmented regime, at resonance, the Schwinger pair creation mechanism still happens, but dynamics are localized within each building block due to confinement. (e) MPS simulation of the confined scarring at $\chi = 0.35\kappa$. The enhancement of scarring in our numerical simulation for the BHM is less clear compared to the PXP model. This is mainly due to the boundary effects, and we expect better results for larger system sizes in the experiment, which is currently beyond the capability of our numerics.

matter is absent. On an even bosonic site, which represents a link of the QLM, zero (two) bosons indicate that the local electric field points down (up). As such, we need to enforce these local occupations in an experiment. This is achieved in the regime of $U, \delta \gg J, \mu$, where Eq. (1) derives from Eq. (14) up to second order in perturbation theory [13, 26].

The dominating terms of Eq. (14) are then diagonal in the on-site bosonic number operator, and can be collected as

$$\hat{H}_d = \sum_{\ell} \left\{ \frac{U}{2} [\hat{n}_{\ell}(\hat{n}_{\ell} - 1) + \hat{n}_{\ell, \ell+1}(\hat{n}_{\ell, \ell+1} - 1)] + \left[(-1)^{\ell} \frac{\chi}{2} - \delta \right] \hat{n}_{\ell, \ell+1} + \Delta [2\ell \hat{n}_{\ell} + (2\ell + 1) \hat{n}_{\ell, \ell+1}] \right\}, \quad (16)$$

where we have resorted to the QLM indexing, which relates to that of Eq. (14) as ℓ corresponding to an even

bosonic site j , while the link between sites ℓ and $\ell+1$ corresponds to $j+1$, the odd (i.e., gauge) site between the even (i.e., matter) sites j and $j+1$. We can now define a “proto-Gauss’s law” with the generator

$$\hat{\mathcal{G}}_{\ell} = (-1)^{\ell} \left[\frac{1}{2} (\hat{n}_{\ell-1, \ell} + \hat{n}_{\ell, \ell+1}) + \hat{n}_{\ell} - 1 \right]. \quad (17)$$

Relating the configurations allowed by Gauss’s law in both the bosonic and QLM representations, we find that $\mu = \delta - U/2$, which we can insert in Eq. (16) and utilize Eq. (17) to get

$$\hat{H}_d = \sum_{\ell} \left\{ \frac{U}{2} [\hat{n}_{\ell}(\hat{n}_{\ell} - 1) + \hat{n}_{\ell, \ell+1}(\hat{n}_{\ell, \ell+1} - 2)] + \left[(-1)^{\ell} \frac{\chi}{2} - \mu \right] \hat{n}_{\ell, \ell+1} + c_{\ell} \hat{\mathcal{G}}_{\ell} \right\}, \quad (18)$$

up to an inconsequential energy constant, with $c_{\ell} = 2\Delta(-1)^{\ell}$. This formulation with the “Stark” co-

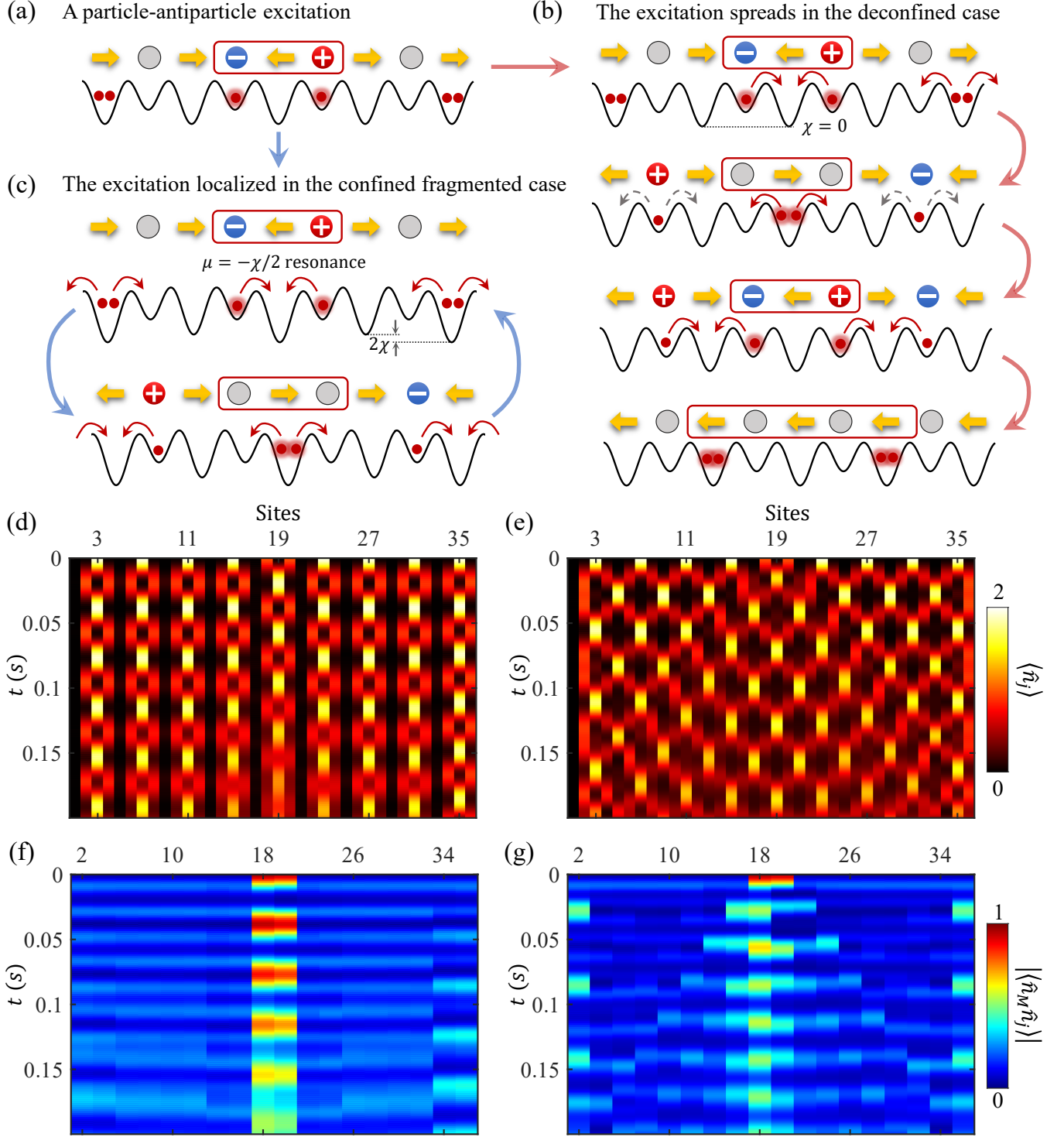


FIG. 10. (Color online). The experimental probe of a particle-antiparticle excitation in the vacuum background. (a) Preparation of the particle-antiparticle excitation in the Bose-Hubbard quantum simulator. (b) Schematic of the coupling between the excitation and the background in the deconfined case. Coupling between the unit cells leads to the spreading of the excitation. (e) and (g): MPS simulation of the light-cone spreading. (e) The particle density, (g) the density-density correlation between a center matter site with the particle and the rest of the matter sites. (c) In the fragmented case, at resonance $\chi = \kappa$, $\mu = -0.5\kappa$, the defect is unable to couple to the neighboring unit cells due to the staggering χ , and is hence unable to spread, resulting in decoupled dynamics between the excitation and the background. (d) and (f): Same simulation as for (e) and (g), for the fragmented case. The excitation is localized due to confinement.

efficients c_ℓ has recently been shown to suppress couplings between different gauge sectors, and hence sta-

bilize gauge invariance, up to all numerically accessible times [83] based on the concept of *linear gauge protection* [84]. Looking at Eq. (18), we see that a large on-site potential constrains the local bosonic configurations on sites to $\{|0\rangle_\ell, |1\rangle_\ell\}$ and on links to $\{|0\rangle_{\ell,\ell+1}, |2\rangle_{\ell,\ell+1}\}$, as desired. The latter correspond to the local eigenstates of the Pauli operator $\hat{\sigma}_\ell^z$ and $\hat{s}_{\ell,\ell+1}^z$ of Eq. (1). In this regime, Eqs. (17) and (2) become equivalent. Using degenerate perturbation theory, the parameters of Eqs. (14) and (1) can be related through

$$\kappa = 2\sqrt{2}J^2 \left[\frac{\delta}{\delta^2 - \Delta^2} + \frac{U - \delta}{(U - \delta)^2 - \Delta^2} \right], \quad (19)$$

where, as mentioned, $\mu = \delta - U/2$ is the fermionic mass.

The extended BHM Hamiltonian (14) can be realized by a three-period optical superlattice formed by standing waves of lasers. The main lattice laser with wavelength λ forms a lattice with period $\lambda/2$, and two additional lattices with period λ and 2λ , respectively. These lasers can be phase stabilized with respect to each other to generate the desired superlattice potential as described in Ref. [26]. The two vacuum states in the gauge theory correspond to states $|00200020\dots\rangle$ and $|20002000\dots\rangle$ in the BHM. They can be prepared with site-selective addressing techniques using the spin-dependent superlattice, also described in Ref. [26].

In keeping with experimental relevance, we have set the microscopic parameters of Hamiltonian (14) to $U = 1368$ Hz, $J = 58$ Hz, and $\Delta = 57$ Hz, which are close to the values of these parameters as employed in the experiment of Ref. [14]. We first investigate the crossover from deconfined scarring to fragmentation. In the deconfined case ($\chi = 0$), when quenching the vacuum state to $\mu = 0$, the system displays scarred dynamics in form of “state transfer” between the two vacuum states, see Fig. 9(b). We obtain the numerical results for the BHM using the TenPy toolkit [85]. The system shows persistent many-body oscillations between the two vacuum states, as can be seen in Fig. 9(d).

When the confinement potential is increased to $\chi = 0.35\kappa$, the system remains ergodic, while scarring from the Néel state persists. This regime of confined scarring is discussed in Sec. III. The transfer to the opposite vacuum state is suppressed due to confinement, but dynamics between the unit cells are still present. However, the enhancement of scarring is not as clear as in the PXP model mainly due to the boundary effects, see Fig. 9(e). We expect the enhancement effect to be better for larger system sizes, as the boundaries become less relevant. But this is currently beyond the capability of our numerics.

The system becomes fragmented when confinement potential χ is above 0.5κ . Here, we use the resonant case with $\chi = \kappa$ and $\mu = -0.5\kappa$ as an example. As shown in Fig. 9(c), unit cells marked in gray shades are tuned on resonance with $\mu = -\chi/2$, while the adjacent unit cells are out-of-resonance. Therefore dynamics are restricted within the unit cells, see the numerical results in Fig. 9(f).

We further propose to probe confinement and fragmentation by investigating the spread of a particle-antiparticle excitation in the vacuum background. In the Bose–Hubbard quantum simulator, this state corresponds to a $|\dots 0101\dots\rangle$ impurity at the center of the $|\dots 0020\dots\rangle$ background, see Fig. 10(a). This state can be prepared by a local addressing operation in the optical superlattice, as described in [26]. In the deconfined case, the excitation couples with neighboring unit cells, see Fig. 10(b). The light-cone spreading can be seen in the numerical results in Fig. 10(e) and (g), calculated numerically using MPS. Additional to the mean density $\langle \hat{n}_j \rangle$ in panel (e), in panel (g) we calculate the density-density correlation between site 18 (a matter site with the excitation) and the rest of the matter sites, $\langle \hat{n}_M \hat{n}_j \rangle$.

In the fragmented case, however, the dynamics are restricted within each unit cell, as we demonstrate for the case $\chi = \kappa$ and $\mu = -0.5\kappa$ in Fig. 10(c). The excitation is disconnected from the rest of the system and goes on its own dynamics, see Fig. 10(d), therefore, no spreading can be observed in the density-density correlation, see Fig. 10(f).

VI. CONCLUSIONS AND OUTLOOK

Using a combination of analytic and numerical methods, we have calculated the dynamical phase diagram of the U(1) quantum link model with a topological θ -term, or equivalently, the PXP model with mass and staggered magnetization terms. By tuning the topological θ -angle on a quantum simulator as recently proposed in Ref. [26], we can controllably induce confinement in this model. Accordingly, we map out various ergodicity-breaking phases that can be observed experimentally by tuning the confining potential χ and the effective mass μ in an cold-atom setup. Starting from the ergodic phase at small values of the mass and confining potential, we study the crossover to the fragmented phase at large χ , and to the integrable phase at large μ . Additionally, we have identified various resonant processes in the (χ, μ) dynamical phase diagram, which we have analyzed in detail. We further uncovered regimes of robust quantum many-body scarring in the presence of confinement.

Our results are readily accessible in modern cold-atom quantum simulators [13, 14] by adding a third staggering potential in the associated tilted Bose–Hubbard optical superlattice. Our findings highlight a very interesting phenomenological and technological aspect. They show that confinement and quantum many-body scarring, two paradigmatic phenomena of gauge theories, can arise concomitantly. Importantly, our results also show that this behavior can be captured on current quantum simulators, which is encouraging given the current drive of probing high-energy physics on table-top quantum devices. Our work also further sheds light on the question of the gauge-theoretic origin of quantum many-body scarring. Previously, scarring and confinement were thought

to arise in completely different regimes, but here we show that they can coexist and give rise to interesting dynamics. Confinement is a fundamentally gauge-theoretic phenomenon, so it is interesting to further investigate the nature of confined scarring in more generic gauge theories such as \mathbb{Z}_2 lattice gauge theories [86] or quantum link models in higher spatial dimensions [61].

ACKNOWLEDGMENTS

J.C.H. acknowledges stimulating discussions with Pablo Sala. The authors are grateful to Aiden Daniel, Andrew Hallam, Philipp Hauke, Ana Hudomal, Jian-Wei Pan, and Zhen-Sheng Yuan for discussions and works on related topics. J.C.H. acknowledges funding from the European Research Council (ERC) under the European Union’s Horizon 2020 research and innovation program (Grant Agreement no 948141) — ERC Starting Grant SimUcQuam, and by the Deutsche Forschungsgemeinschaft (DFG, German Research Foundation) under Germany’s Excellence Strategy – EXC-2111 – 390814868. I.P.M. acknowledges support from the Australian Research Council (ARC) Discovery Project Grants No. DP190101515 and DP200103760. J.-Y.D. and Z.P. acknowledge support by EPSRC grant EP/R513258/1 and by the Leverhulme Trust Research Leadership Award RL-2019-015. Statement of compliance with EPSRC policy framework on research data: This publication is theoretical work that does not require supporting research data.

Appendix A: Level statistics with μ and χ

In order to identify non-ergodic regimes, we can resort to computing level-spacing statistics, and in particular the $\langle r \rangle$ value. This is only meaningful once symmetries have been resolved, and we consider this quantity only in the most symmetric sector. The relevant symmetries and the sector will change depending whether μ and χ are zero or not. Let us denote the translation operator by \hat{T} and the spatial inversion operator by \hat{L} . When $\chi = 0$, the Hamiltonian commutes with both \hat{T} and \hat{L} , and we consider the symmetry sector with momentum $k = 0$ and spatial inversion eigenvalue $p = +1$. When $\chi \neq 0$, the Hamiltonian no longer commutes with either \hat{T} nor \hat{L} (as we consider even system sizes). However it does commute with \hat{T}^2 and $\hat{T}\hat{L}$. Just as \hat{T} and \hat{L} commute in the zero-momentum sector, \hat{T}^2 and $\hat{T}\hat{L}$ commute when the momentum k_2 (with respect to \hat{T}^2) is 0. So in these cases we focus on the symmetry sector $k_2 = 0$ and $p_T = +1$. Finally, as shown in SM [73], when $\mu = 0$ the Hamiltonian has a particle-hole symmetry and consequently a large number of zero modes. So we always truncate the spectrum to remove these modes. We also remove the edges of the spectrum.

Once these symmetries have been resolved, for small value of μ and χ we expect the system to consist of a single connected component with a non-integrable Hamiltonian. But when fragmentation sets in, we then have several disconnected sectors that do not have level repulsion between them. We have also seen that away from resonances the effective Hamiltonian at second order is non-interacting and so trivially integrable. As such we expect a quick departure from Wigner-Dyson level statistics as soon as fragmentation starts to occur. Figure 11 shows that a value of χ of $\sim 0.5\kappa$ is enough to break ergodicity for 26 sites. We note that for such values of χ/κ , the energy spacing between sectors is not many orders of magnitudes larger than the intra-sector spacing. Following a quench, we see the wave function spreading into other sectors after a finite time that grows with χ/κ . Hence we dub this regime “prethermal fragmented.”

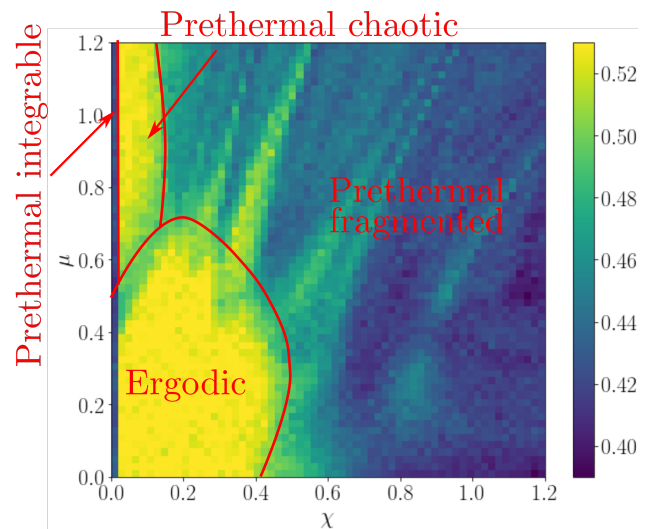


FIG. 11. (Color online). Level spacing statistics in the PXP model with PBC with $L_m = 28$. All values below 0.39 are set to this value and all values above 0.53 are set to 0.53. The red lines show the approximate limits between the different regimes.

This is confirmed on Fig. 12 that shows the scaling of the r ratio for various values of χ and L_m . As expected, a larger perturbation is needed to induce fragmentation as L_m is increased. Going away from $\mu = 0$, we see a non-monotonic behavior of $\langle r \rangle$ as χ is increased. This is manifested by the lighter “rays” emanating from region I and into region IV of Fig. 11. These seemingly special ergodic lines are also visible on the top panel of Fig. 13, which show the influence of χ for various fixed μ (with a finer χ resolution than Fig. 11). In order to show that these regions are not ergodic either, we will concentrate on the case with $\mu = 0.8$ and $\chi = 0.385$, which correspond to a local maximum of $\langle r \rangle$ for that value of μ . We compute the integrated density of states

$$G(\epsilon) = \frac{1}{D} \sum_E \Theta(\epsilon - E), \quad (\text{A1})$$

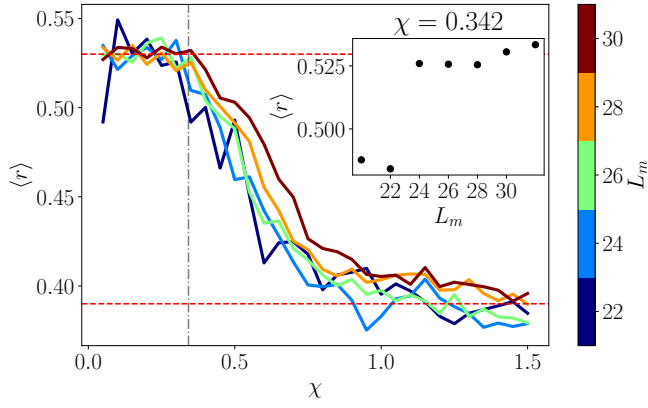


FIG. 12. (Color online). Level spacing statistics in the PXP model with PBC and $\mu = 0$. Each colored curve corresponds to a different system size. The red dashed lines indicated the expected values for Poisson and Wigner-Dyson distributions. The inset shows the system size scaling at the optimal value of χ to maximize revivals from the Néel state.

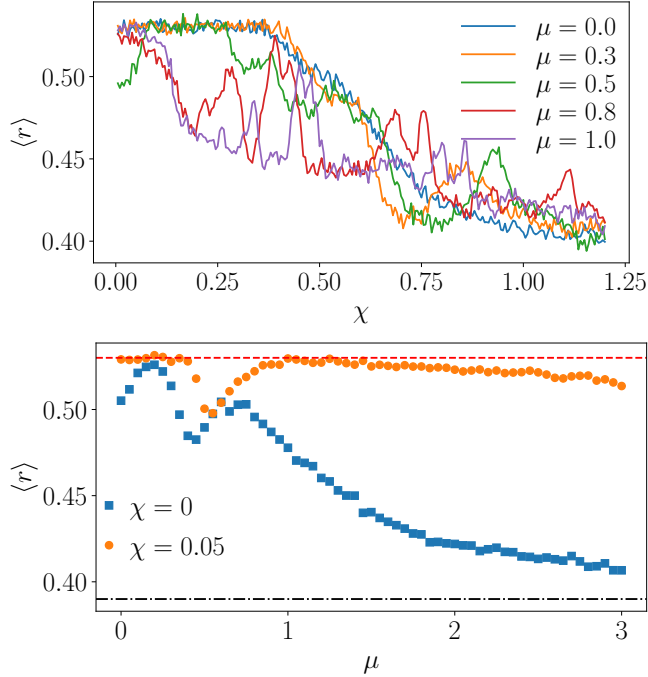


FIG. 13. (Color online). Level spacing statistics in the PXP model with PBC with $L_m = 30$. Top: Each curve corresponds to a fixed value of μ . The values for $\chi = 0$ are not included as they have different symmetries. As μ is increased, a lower value of χ is needed to deviate from 0.53. For $\mu \geq 0.5$, one can see peaks in the r value. However further investigation shows that these regimes are not truly ergodic either. Bottom: Results for various values of μ with fixed χ . Note that both cases have different spatial symmetries, which are resolved.

which simply counts what fraction of energy levels lies below energy ϵ . For a fully chaotic system in which symmetries have been resolved, we expect this function to be

smooth. However plotting G for $\mu = 0.8$ and $\chi = 0.385$ as in Fig. 14(a) shows clear plateaus, indicating gaps where no levels are found. If we now consider each set of eigen-

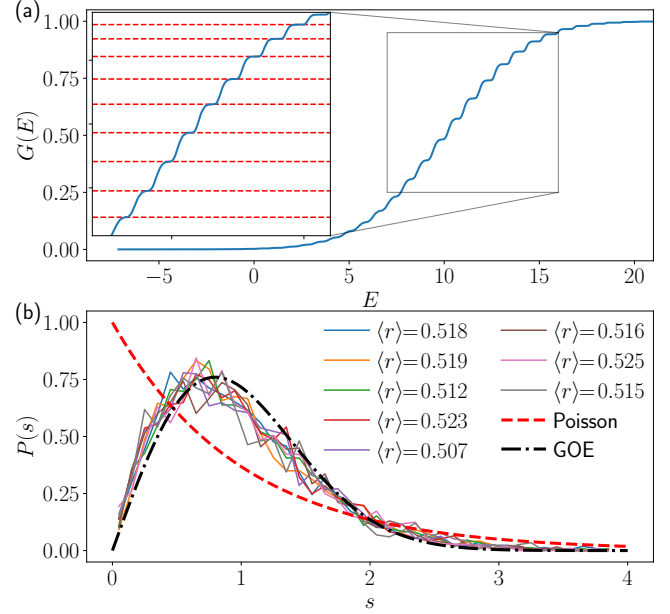


FIG. 14. (Color online). Level spacing statistics in the PXP model with PBC with $L_m = 28$ for $\mu = 0.8$ and $\chi = 0.385$. The staircase-like behavior of $G(E)$ in (a) is emblematic of the presence of sectors with many energy levels separated by empty intervals where $G(E)$ does not grow. The red dashed lines in the inset indicate the fraction of eigenstates chosen as limits between sectors. In each sector the spectrum was then unfolded and the probability distribution of level spacings s was plotted in (b).

states between the flat plateaus as independent spectra, we can unfold them and plot the distribution of level spacings as in Fig. 14(b). They show good agreement with the Wigner surmise, and consequently the $\langle r \rangle$ value is close to 0.53. However, due to this splitting into bands, the full system is clearly not ergodic. Thus, we understand the non-uniformity of region IV in Fig. 11 as the result of interplay between disconnected components. Indeed, the first few orders of the effective Hamiltonian for generic μ and χ do not connect the entire Hilbert space together. So for large enough values of these parameters, we will end up with an extensive number of disconnected components that can be diagonalized independently. Each of these will have energies centered around some energy \bar{E} , which depends on μ and χ . Around resonances, several disconnected components can end up close in energies. This can happen without them becoming connected in the low-order terms of the effective Hamiltonian. In that case, their energy levels will mix, thus impacting the energy spacing and the average $\langle r \rangle$ value. This will lead to lower $\langle r \rangle$ value, as in the case of unresolved symmetries.

For μ the picture is different, as even for $\mu = 1.2$

and $\chi = 0.1$ the $\langle r \rangle$ value is close to 0.53. However further investigation shows that this does not indicate the Hamiltonian is fully ergodic. Indeed, for a small χ and a large μ the dominant Hamiltonian is in the one in Eq. (S19), which is non-integrable for any nonzero χ . We still have $L_m/2 + 1$ U(1) sectors (corresponding to the total excitation number), but they are very far apart energy due to μ being large. So their energies do not overlap and as such do not create any accidental degeneracies (or near-degeneracies). The level spacing statistics is dominated by the spacings *within* each sector, which all obey Wigner-Dyson distribution. Hence starting in a sector will lead to prethermalization within that sector for an exponential long time depending on μ/κ , before then starting to explore the other ones. This means that at short and intermediate times, for the system size investigated, the dynamics will only explore a part of the system and so it is non-ergodic. If instead $\chi = 0$, then the Hamiltonian in each U(1) sector is integrable and we see much faster convergence towards Poissonian statistics with μ (see bottom panel of Fig. 13). Nonetheless, as we have noted above, for $\mu \gg \chi, \kappa$ there is an emergent U(1) conservation law at short and intermediate time but no fragmentation within each U(1) sector.

Appendix B: Algebra enhancement for $\mu = 0$

In this section, we show how the confining potential χ leads to an enhancement of the su(2) algebra linked to QMBS from the Néel state. In order to understand the origin of the non-monotonicity of scarring with χ , we can look at the properties of the top band of states. To do that we algorithmically identify them for various values of χ between 0 and 0.5 based on their energies and overlap with the Néel state. In this regime we still see relatively clear towers of states throughout the spectrum with a state at the top that is well separated from the rest. On Fig. 15, we show that the total overlap between these states and the Néel state has a local maximum around $\chi = 0.34$. At the same time, the standard deviation of the level spacings between consecutive eigenstates in the top band has a minimum around $\chi = 0.28$. Both of these phenomena are expected to lead to better revivals, and would also generally indicate that the approximate su(2) algebra obeyed by the scarred state is “closer” to be exact.

In order to show this in a more quantitative way, we turn to the forward scattering approximation (FSA) [50]. This method allows to construct approximations to the $L_m + 1$ state in the top band. This completely removes the problem of eigenstate hybridization and the risk of error in the identification of the top band states. We decompose the Hamiltonian in three parts as

$$\hat{H} = \hat{H}^+ + \hat{H}^- + \hat{H}^Z, \quad (\text{B1})$$

where $\hat{H}^+ = \sum_{j=1}^{L_m/2} \hat{s}_{2j-1}^+ + \hat{s}_{2j}^-$, $\hat{H}^- = (\hat{H}^+)^{\dagger}$ and $\hat{H}^Z =$

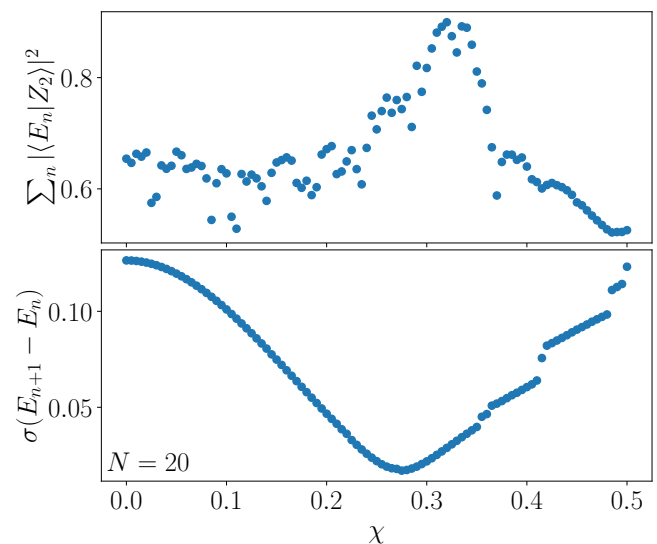


FIG. 15. (Color online). Properties of the top band of $N + 1$ scarred eigenstates in the PXP with $L_m = 20$. Top: total overlap between the scarred states and the Néel state. Bottom: standard deviation of the spacing between consecutive scarred eigenstates. As the scarred eigenstates were detected algorithmically using the energy and overlap with the Néel state, it might not be totally accurate for all values of χ .

$\sum_l (-1)^l \chi \hat{s}_l^z$ is the diagonal part. We form the FSA basis states using \hat{H}^+ , and as such these are the same for any value of χ . All states in the FSA basis are eigenstates of \hat{H}^z , and so this operator is perfectly captured by this approximation. These two facts mean that the energy subspace variance of the FSA does not vary with χ , and so it cannot be used as a metric for the algebra being correct.

We form the FSA basis states by starting from the Néel state and applying \hat{H}^+ . This means that the basis state $|F_k\rangle \propto (\hat{H}^+)^k |Z_2\rangle$. The procedure terminates at $|F_{L_m}\rangle$ as applying \hat{H}^+ to this state annihilates it. This construction produces the same basis states for any value of χ , including $\chi = 0$. All $|F_k\rangle$ are eigenstates of \hat{H}^z , so this operator is perfectly captured by this approximation and only adds a diagonal term to the FSA Hamiltonian. This gives us a relatively simple picture, with a tridiagonal Hamiltonian where only the diagonal depends on χ .

Nonetheless, we can still compute the revivals and the standard deviation of the eigenstate spacing in the FSA subspace up to $L_m = 100$. This is shown on Fig. 16 and is very similar to results in the full system. The simpler form of the FSA Hamiltonian (a tridiagonal matrix), also allow us to get a clearer picture of how the algebra is improved by the χ term. Indeed, if the algebra was exact, the β_n on the off diagonal should obey $\beta_n = \lambda \sqrt{(n+1)(N-n)}$, where λ is an overall strength factor. We can match the off-diagonal couplings of PXP for $n = 1, 2, N-2$ and $N-1$ by setting $\lambda = 1/\sqrt{2}$.

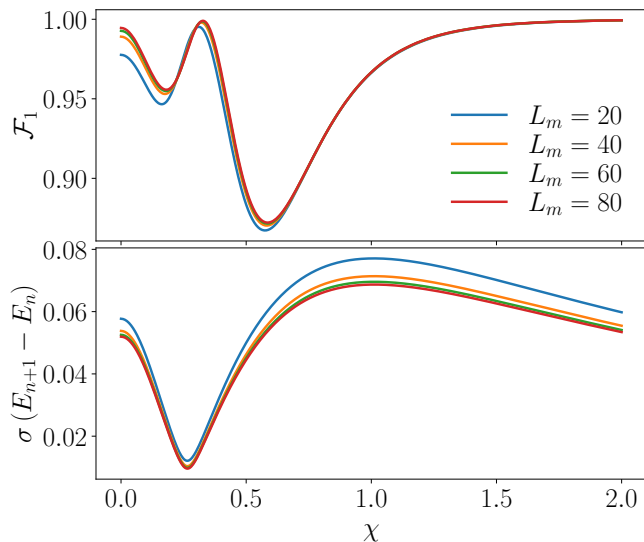


FIG. 16. (Color online). Properties of the FSA eigenstates for various system sizes. Both the best revival fidelity and the most equal energy spacing show optimal points between 0.3 and 0.5.

However the middle couplings are too low in strength. As stated before, adding a nonzero χ does not modify these off-diagonal couplings but add diagonal terms $\alpha_n = -\chi(N - n)$. In order to visualize the effect of χ on the algebra, we can get rid of the diagonal entries through a change of basis. Indeed, if the algebra was exact, the FSA matrix would simply be $\frac{1}{\sqrt{2}}\hat{S}^x + \chi\hat{S}^z$ and applying a rotation of angle $\theta = \tan^{-1}(\sqrt{2}\chi)$ around the Y axis would change it to $\sqrt{1/2 + \chi^2}\hat{S}^x$.

As the algebra is not exact, this is no longer the case. However, we find that there is an optimal angle θ^* that still leads to a matrix that has large entries on the two off-diagonals and small values everywhere else. For each χ , we find the optimal θ^* such that the norm of the diagonal is minimized. The value of the off-diagonal couplings β_n will then vary with χ , and we can compare them to those of the spin matrix \hat{S}^x that would lead to perfect revivals. Figure 17 shows this for $L_m = 100$ and for a large range of χ . For small values of χ , the middle couplings rise faster than the edge ones, and thus “correct” the former that are lower than the exact $\text{su}(2)$ ones, before overshooting. Once χ becomes large, the edge couplings start to catch up, and will match the $\text{su}(2)$ ones in the limit of $\chi \rightarrow \infty$.

The other point where the β_n couplings resemble the $\text{su}(2)$ ones the most are around $\chi = 0.4$, this can be seen more clearly on Fig. 18. In order to make sure that the matrix obtained after the change basis only has nonzero matrix elements on the upper and lower diagonals, we can look at the ration of its norm with and without these elements. This is shown on Fig. 18, and the results are of the order of 1% for all χ . Importantly, these undesired couplings are minimal for $\chi = 0$ and $\chi = \infty$. The competition of these various minima creates the picture that

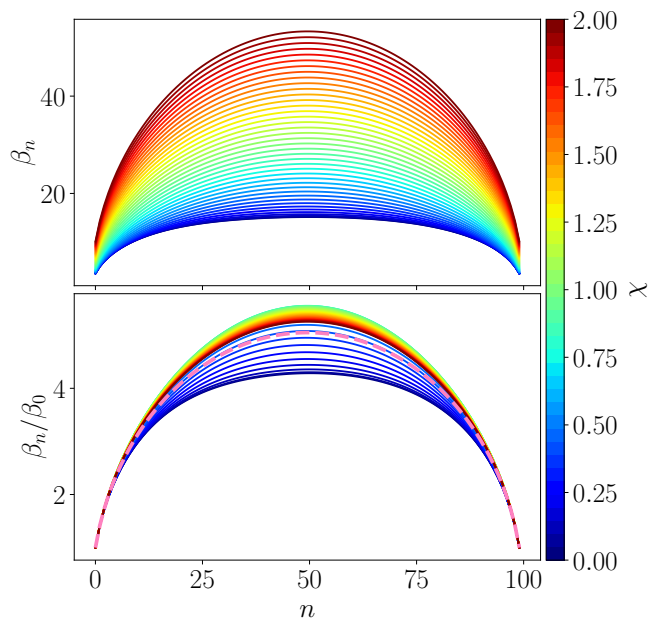


FIG. 17. (Color online). Upper and lower diagonal couplings of the FSA Hamiltonian after rotation for $L_m = 100$. The pink curve in the lower panel corresponds to the couplings for an exact $\text{su}(2)$ algebra. The

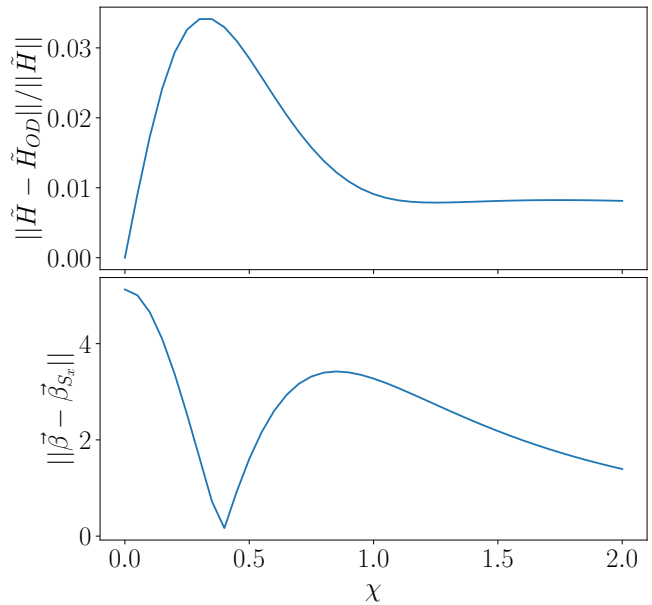


FIG. 18. (Color online). Properties of the FSA Hamiltonian after rotation for $L_m = 100$. Top panel: ratio between the norm of the matrix without the upper- and lower-diagonal, and with it. This quantity is low for all values of χ , showing that the matrix is close to a tridiagonal one. Bottom panel:

we see in the full model, with revival peaking at $\chi = 0$, $\chi \approx 0.35$, and $\chi \rightarrow \infty$.

We note that other more complex approximation schemes can also be used to study the nonmonotonic

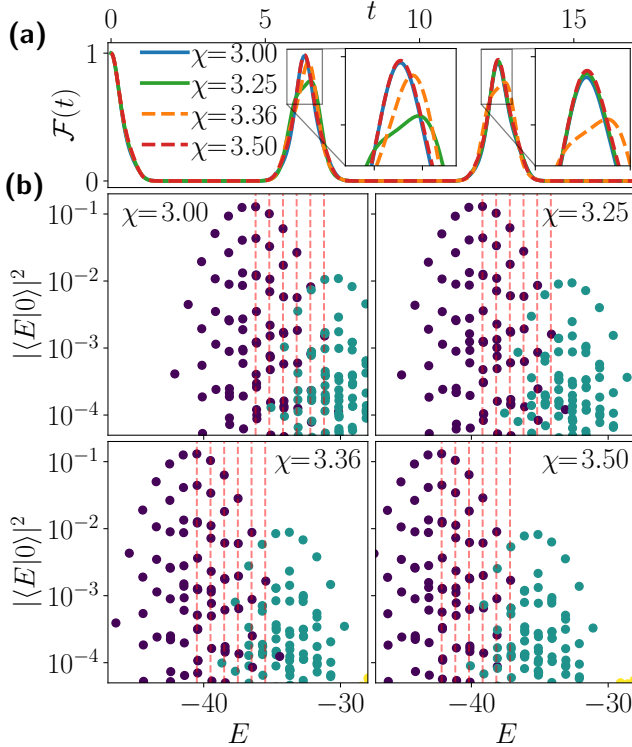


FIG. 19. (Color online). Quenches from the polarized state in the PXP model with $L_m = 24$ along the resonance line $\chi = -2\mu$. (a) Self-fidelity after a quench. When χ is integer or half-integer, the first peak is significantly higher. (b) Overlap between polarized state and the eigenstates. The color indicates the number of excitations on odd sites and so differentiates states in different sectors. The red dashed-lines are all equally spaced by one unit of energy. When χ is integer or half-integer, the spacing between sectors is a multiple of the energy spacing within each of them and all eigenstates are approximately equally spaced.

behavior in χ . In the SM [73], we use the symmetric subspace approximation [87] which captures more states than the FSA. Another advantage of this approximation is that it allows to get the classical limit for the dynamics from the Néel state. Even in this case, the same non-monotonic behavior with respect to χ can be witnessed, showing the strong robustness of this effect.

Appendix C: Polarized state at $\chi \approx \pm 2\mu$

At the resonance point $\chi \approx -2\mu$, the Hilbert space fractures when $\chi, \mu \gg \kappa$ as creating an excitation on an odd site is extremely costly in energy. However when $1 < \chi/\kappa < 10$ such moves are still possible from the polarized states. As a consequence, the dynamics is not restricted to the Hilbert space sector with no excitations on the even sites, but the sector with one excitation of these sites also has some nonzero contribution. For a detuning $\gamma = 2\mu + \chi$, the Hamiltonian in each fragment

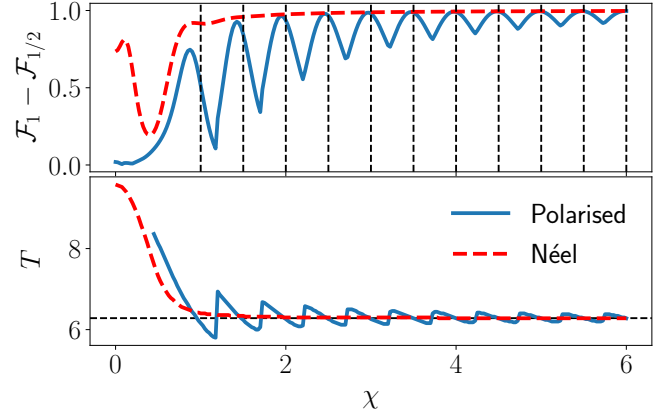


FIG. 20. (Color online). Self-fidelity and period of revival in the PXP model with $L_m = 22$ along the resonance line $\chi = -2\mu$ for the polarized and Néel states. As χ gets large, contributions from sectors with excitations on odd sites become smaller and the further resonance condition for χ to be integer or half-integer matters less.

is given by Eq. (9) in the main text. It is straightforward to see that the energy spacing between eigenstates in that system is $\sqrt{1 + \gamma^2}$ for $\kappa = 1$. Meanwhile, the energy spacing between the “center” of fragments with respectively 0 and 1 excitations on odd sites is largely unaffected by γ and is approximately 2χ . As a consequence, in order for all energies to be spaced by a regular amount we require one of these quantities to be a multiple of the other. As $\chi \gg \gamma$, it must be that $2\chi > \sqrt{1 + \gamma^2}$ and so the condition can be expressed as

$$\chi = \frac{n\sqrt{1 + \gamma^2}}{2}, \quad \mu = \frac{\gamma - \chi}{2} \quad (\text{C1})$$

with n an integer. Alternatively, one can combine both equations to remove γ and get

$$\frac{(2\chi)^2}{n^2} - (2\mu + \chi)^2 = 1, \quad (\text{C2})$$

which parametrizes a hyperbola. There is such a hyperbola for any n , although the agreement gets better as n increases as the condition $\mu, \chi \gg \gamma, \kappa$ is better satisfied. At the same time, points between hyperbolas also get better revivals between as μ and χ increase. This is best seen on the resonance line $\gamma = 0$. In that case, the additional condition for energies to align is simply to require χ to be half-integer or integer multiples of κ , as the spacing within each sector is simply κ . The effect of this can be seen on Fig. 19 for $\kappa = 1$. When the condition is met, the polarized state revives with period 2π .

One can monitor that period as well as the fidelity at the first revival as $\chi = 2\mu$ is increased. Figure 20 shows this for the Néel and polarized states. As expected, the fidelity gets better as χ is increased because other Hilbert space sectors are more suppressed.

- [1] S. Weinberg, *The Quantum Theory of Fields*, Vol. 2: Modern Applications (Cambridge University Press, 1995).
- [2] C. Gatttringer and C. Lang, *Quantum Chromodynamics on the Lattice: An Introductory Presentation*, Lecture Notes in Physics (Springer Berlin Heidelberg, 2009).
- [3] A. Zee, *Quantum Field Theory in a Nutshell* (Princeton University Press, 2003).
- [4] Esteban A. Martinez, Christine A. Muschik, Philipp Schindler, Daniel Nigg, Alexander Erhard, Markus Heyl, Philipp Hauke, Marcello Dalmonte, Thomas Monz, Peter Zoller, and Rainer Blatt, “Real-time dynamics of lattice gauge theories with a few-qubit quantum computer,” *Nature* **534**, 516–519 (2016).
- [5] Christine Muschik, Markus Heyl, Esteban Martinez, Thomas Monz, Philipp Schindler, Berit Vogell, Marcello Dalmonte, Philipp Hauke, Rainer Blatt, and Peter Zoller, “U(1) Wilson lattice gauge theories in digital quantum simulators,” *New Journal of Physics* **19**, 103020 (2017).
- [6] Hannes Bernien, Sylvain Schwartz, Alexander Keesling, Harry Levine, Ahmed Omran, Hannes Pichler, Soonwon Choi, Alexander S. Zibrov, Manuel Endres, Markus Greiner, Vladan Vuletić, and Mikhail D. Lukin, “Probing many-body dynamics on a 51-atom quantum simulator,” *Nature* **551**, 579–584 (2017).
- [7] N. Klco, E. F. Dumitrescu, A. J. McCaskey, T. D. Morris, R. C. Pooser, M. Sanz, E. Solano, P. Lougovski, and M. J. Savage, “Quantum-classical computation of Schwinger model dynamics using quantum computers,” *Phys. Rev. A* **98**, 032331 (2018).
- [8] C. Kokail, C. Maier, R. van Bijnen, T. Brydges, M. K. Joshi, P. Jurcevic, C. A. Muschik, P. Silvi, R. Blatt, C. F. Roos, and P. Zoller, “Self-verifying variational quantum simulation of lattice models,” *Nature* **569**, 355–360 (2019).
- [9] Christian Schweizer, Fabian Grusdt, Moritz Berngruber, Luca Barbiero, Eugene Demler, Nathan Goldman, Immanuel Bloch, and Monika Aidelsburger, “Floquet approach to \mathbb{Z}_2 lattice gauge theories with ultracold atoms in optical lattices,” *Nature Physics* **15**, 1168–1173 (2019).
- [10] Frederik Görg, Kilian Sandholzer, Joaquín Minguzzi, Rémi Desbuquois, Michael Messer, and Tilman Esslinger, “Realization of density-dependent Peierls phases to engineer quantized gauge fields coupled to ultracold matter,” *Nature Physics* **15**, 1161–1167 (2019).
- [11] Alexander Mil, Torsten V. Zache, Apoorva Hegde, Andy Xia, Rohit P. Bhatt, Markus K. Oberthaler, Philipp Hauke, Jürgen Berges, and Fred Jendrzejewski, “A scalable realization of local u(1) gauge invariance in cold atomic mixtures,” *Science* **367**, 1128–1130 (2020).
- [12] Natalie Klco, Martin J. Savage, and Jesse R. Stryker, “SU(2) non-abelian gauge field theory in one dimension on digital quantum computers,” *Phys. Rev. D* **101**, 074512 (2020).
- [13] Bing Yang, Hui Sun, Robert Ott, Han-Yi Wang, Torsten V. Zache, Jad C. Halimeh, Zhen-Sheng Yuan, Philipp Hauke, and Jian-Wei Pan, “Observation of gauge invariance in a 71-site Bose–Hubbard quantum simulator,” *Nature* **587**, 392–396 (2020).
- [14] Zhao-Yu Zhou, Guo-Xian Su, Jad C. Halimeh, Robert Ott, Hui Sun, Philipp Hauke, Bing Yang, Zhen-Sheng Yuan, Jürgen Berges, and Jian-Wei Pan, “Thermalization dynamics of a gauge theory on a quantum simulator,” *Science* **377**, 311–314 (2022).
- [15] Nhung H. Nguyen, Minh C. Tran, Yingyue Zhu, Alaina M. Green, C. Huerta Alderete, Zohreh Davoudi, and Norbert M. Linke, “Digital quantum simulation of the Schwinger model and symmetry protection with trapped ions,” *PRX Quantum* **3**, 020324 (2022).
- [16] Zhan Wang, Zi-Yong Ge, Zhongcheng Xiang, Xiaohui Song, Rui-Zhen Huang, Pengtao Song, Xue-Yi Guo, Luhong Su, Kai Xu, Dongning Zheng, and Heng Fan, “Observation of emergent \mathbb{Z}_2 gauge invariance in a superconducting circuit,” *Phys. Rev. Research* **4**, L022060 (2022).
- [17] Julius Mildenerberger, Wojciech Mruczkiewicz, Jad C. Halimeh, Zhang Jiang, and Philipp Hauke, “Probing confinement in a \mathbb{Z}_2 lattice gauge theory on a quantum computer,” arXiv e-prints (2022), [arXiv:2203.08905 \[quant-ph\]](https://arxiv.org/abs/2203.08905).
- [18] Yuri Alexeev, Dave Bacon, Kenneth R. Brown, Robert Calderbank, Lincoln D. Carr, Frederic T. Chong, Brian DeMarco, Dirk Englund, Edward Farhi, Bill Fefferman, Alexey V. Gorshkov, Andrew Houck, Jungsang Kim, Shelby Kimmel, Michael Lange, Seth Lloyd, Mikhail D. Lukin, Dmitri Maslov, Peter Maunz, Christopher Monroe, John Preskill, Martin Roetteler, Martin J. Savage, and Jeff Thompson, “Quantum computer systems for scientific discovery,” *PRX Quantum* **2**, 017001 (2021).
- [19] Natalie Klco, Alessandro Roggero, and Martin J. Savage, “Standard model physics and the digital quantum revolution: thoughts about the interface,” *Reports on Progress in Physics* **85**, 064301 (2022).
- [20] M. Dalmonte and S. Montangero, “Lattice gauge theory simulations in the quantum information era,” *Contemporary Physics* **57**, 388–412 (2016).
- [21] Erez Zohar, J Ignacio Cirac, and Benni Reznik, “Quantum simulations of lattice gauge theories using ultracold atoms in optical lattices,” *Reports on Progress in Physics* **79**, 014401 (2015).
- [22] Monika Aidelsburger, Luca Barbiero, Alejandro Bermudez, Titas Chanda, Alexandre Dauphin, Daniel González-Cuadra, Przemysław R. Grzybowski, Simon Hands, Fred Jendrzejewski, Johannes Jünemann, Gediminas Juzeliūnas, Valentin Kasper, Angelo Piga, Shi-Ju Ran, Matteo Rizzi, Germán Sierra, Luca Tagliacozzo, Emanuele Tirrito, Torsten V. Zache, Jakub Zakrzewski, Erez Zohar, and Maciej Lewenstein, “Cold atoms meet lattice gauge theory,” *Philosophical Transactions of the Royal Society A: Mathematical, Physical and Engineering Sciences* **380**, 20210064 (2022).
- [23] Erez Zohar, “Quantum simulation of lattice gauge theories in more than one space dimension—requirements, challenges and methods,” *Philosophical Transactions of the Royal Society of London Series A* **380**, 20210069 (2022).
- [24] Christian W. Bauer, Zohreh Davoudi, A. Baha Balantekin, Tanmoy Bhattacharya, Marcela Carena, Wibe A. de Jong, Patrick Draper, Aida El-Khadra, Nate Gemelke, Masanori Hanada, Dmitri Kharzeev, Henry Lamm, Ying-Ying Li, Junyu Liu, Mikhail Lukin, Yannick Meurice, Christopher Monroe, Benjamin Nachman, Guido Pagano, John Preskill, Enrico Rinaldi, Alessandro Roggero, David I. Santiago, Martin J. Savage, Irfan Siddiqi,

- George Siopsis, David Van Zanten, Nathan Wiebe, Yukari Yamauchi, Kübra Yeter-Aydeniz, and Silvia Zorzetti, “Quantum simulation for high energy physics,” arXiv e-prints (2022), [arXiv:2204.03381 \[quant-ph\]](https://arxiv.org/abs/2204.03381).
- [25] Simon Catterall, Roni Harnik, Veronika E. Hubeny, Christian W. Bauer, Asher Berlin, Zohreh Davoudi, Thomas Faulkner, Thomas Hartman, Matthew Headrick, Yonatan F. Kahn, Henry Lamm, Yannick Meurice, Surjeet Rajendran, Mukund Rangamani, and Brian Swingle, “Report of the Snowmass 2021 theory frontier topical group on quantum information science,” arXiv e-prints (2022), [arXiv:2209.14839 \[quant-ph\]](https://arxiv.org/abs/2209.14839).
- [26] Jad C. Halimeh, Ian P. McCulloch, Bing Yang, and Philipp Hauke, “Tuning the topological θ -angle in cold-atom quantum simulators of gauge theories,” arXiv e-prints (2022), [arXiv:2204.06570 \[cond-mat.quant-gas\]](https://arxiv.org/abs/2204.06570).
- [27] Yanting Cheng, Shang Liu, Wei Zheng, Pengfei Zhang, and Hui Zhai, “Tunable confinement-deconfinement transition in an ultracold atom quantum simulator,” arXiv e-prints (2022), [arXiv:2204.06586 \[cond-mat.quant-gas\]](https://arxiv.org/abs/2204.06586).
- [28] Boye Buyens, Jutho Haegeman, Henri Verschelde, Frank Verstraete, and Karel Van Acoleyen, “Confinement and string breaking for $q\mathbb{Z}_2$ in the hamiltonian picture,” *Phys. Rev. X* **6**, 041040 (2016).
- [29] Federica M. Surace, Paolo P. Mazza, Giuliano Giudici, Alessio Lerose, Andrea Gambassi, and Marcello Dalmonte, “Lattice gauge theories and string dynamics in Rydberg atom quantum simulators,” *Phys. Rev. X* **10**, 021041 (2020).
- [30] T. M. R. Byrnes, P. Sriganesh, R. J. Bursill, and C. J. Hamer, “Density matrix renormalization group approach to the massive Schwinger model,” *Phys. Rev. D* **66**, 013002 (2002).
- [31] Boye Buyens, Jutho Haegeman, Karel Van Acoleyen, Henri Verschelde, and Frank Verstraete, “Matrix product states for gauge field theories,” *Phys. Rev. Lett.* **113**, 091601 (2014).
- [32] Yuya Shimizu and Yoshinobu Kuramashi, “Critical behavior of the lattice schwinger model with a topological term at $\theta = \pi$ using the grassmann tensor renormalization group,” *Phys. Rev. D* **90**, 074503 (2014).
- [33] Matjaž Kebrič, Luca Barbiero, Christian Reinmoser, Ulrich Schollwöck, and Fabian Grusdt, “Confinement and mott transitions of dynamical charges in one-dimensional lattice gauge theories,” *Phys. Rev. Lett.* **127**, 167203 (2021).
- [34] Sidney Coleman, “More about the massive Schwinger model,” *Annals of Physics* **101**, 239 – 267 (1976).
- [35] A. Smith, J. Knolle, D. L. Kovrizhin, and R. Moessner, “Disorder-free localization,” *Phys. Rev. Lett.* **118**, 266601 (2017).
- [36] Marlon Brenes, Marcello Dalmonte, Markus Heyl, and Antonello Scardicchio, “Many-body localization dynamics from gauge invariance,” *Phys. Rev. Lett.* **120**, 030601 (2018).
- [37] A. Smith, J. Knolle, R. Moessner, and D. L. Kovrizhin, “Absence of ergodicity without quenched disorder: From quantum disentangled liquids to many-body localization,” *Phys. Rev. Lett.* **119**, 176601 (2017).
- [38] Alexandros Metavitsiadis, Angelo Pidotella, and Wolfram Brenig, “Thermal transport in a two-dimensional z_2 spin liquid,” *Phys. Rev. B* **96**, 205121 (2017).
- [39] Adam Smith, Johannes Knolle, Roderich Moessner, and Dmitry L. Kovrizhin, “Dynamical localization in \mathbb{Z}_2 lattice gauge theories,” *Phys. Rev. B* **97**, 245137 (2018).
- [40] Angelo Russomanno, Simone Notarnicola, Federica Maria Surace, Rosario Fazio, Marcello Dalmonte, and Markus Heyl, “Homogeneous floquet time crystal protected by gauge invariance,” *Phys. Rev. Research* **2**, 012003 (2020).
- [41] Irene Papaefstathiou, Adam Smith, and Johannes Knolle, “Disorder-free localization in a simple $u(1)$ lattice gauge theory,” *Phys. Rev. B* **102**, 165132 (2020).
- [42] Paul A. McClarty, Masudul Haque, Arnab Sen, and Johannes Richter, “Disorder-free localization and many-body quantum scars from magnetic frustration,” *Phys. Rev. B* **102**, 224303 (2020).
- [43] Oliver Hart, Sarang Gopalakrishnan, and Claudio Castelnovo, “Logarithmic entanglement growth from disorder-free localization in the two-leg compass ladder,” *Phys. Rev. Lett.* **126**, 227202 (2021).
- [44] Guo-Yi Zhu and Markus Heyl, “Subdiffusive dynamics and critical quantum correlations in a disorder-free localized kitaev honeycomb model out of equilibrium,” *Phys. Rev. Research* **3**, L032069 (2021).
- [45] John Sous, Benedikt Kloss, Dante M. Kennes, David R. Reichman, and Andrew J. Millis, “Phonon-induced disorder in dynamics of optically pumped metals from nonlinear electron-phonon coupling,” *Nature Communications* **12**, 5803 (2021).
- [46] P. Karpov, R. Verdel, Y.-P. Huang, M. Schmitt, and M. Heyl, “Disorder-free localization in an interacting 2d lattice gauge theory,” *Phys. Rev. Lett.* **126**, 130401 (2021).
- [47] Nilotpal Chakraborty, Markus Heyl, Petr Karpov, and Roderich Moessner, “Disorder-free localization transition in a two-dimensional lattice gauge theory,” arXiv e-prints, [arXiv:2203.06198 \(2022\)](https://arxiv.org/abs/2203.06198), [arXiv:2203.06198 \[cond-mat.dis-nn\]](https://arxiv.org/abs/2203.06198).
- [48] Jad C. Halimeh, Philipp Hauke, Johannes Knolle, and Fabian Grusdt, “Temperature-induced disorder-free localization,” arXiv e-prints (2022), [arXiv:2206.11273 \[cond-mat.dis-nn\]](https://arxiv.org/abs/2206.11273).
- [49] Sanjay Moudgalya, Stephan Rachel, B. Andrei Bernevig, and Nicolas Regnault, “Exact excited states of nonintegrable models,” *Phys. Rev. B* **98**, 235155 (2018).
- [50] C. J. Turner, A. A. Michailidis, D. A. Abanin, M. Serbyn, and Z. Papić, “Weak ergodicity breaking from quantum many-body scars,” *Nature Physics* **14**, 745–749 (2018).
- [51] Pablo Sala, Tibor Rakovszky, Ruben Verresen, Michael Knap, and Frank Pollmann, “Ergodicity breaking arising from hilbert space fragmentation in dipole-conserving hamiltonians,” *Phys. Rev. X* **10**, 011047 (2020).
- [52] Vedika Khemani, Michael Hermele, and Rahul Nandkishore, “Localization from hilbert space shattering: From theory to physical realizations,” *Phys. Rev. B* **101**, 174204 (2020).
- [53] Luca D’Alessio, Yariv Kafri, Anatoli Polkovnikov, and Marcos Rigol, “From quantum chaos and eigenstate thermalization to statistical mechanics and thermodynamics,” *Advances in Physics* **65**, 239–362 (2016), <https://doi.org/10.1080/00018732.2016.1198134>.
- [54] Joshua M Deutsch, “Eigenstate thermalization hypothesis,” **81**, 082001 (2018).
- [55] Berislav Buča, “Unified theory of local quantum many-body dynamics: Eigenoperator thermalization theorems,” (2023), [10.48550/ARXIV.2301.07091](https://arxiv.org/abs/2301.07091).
- [56] S Chandrasekharan and U.-J Wiese, “Quantum link models: A discrete approach to gauge theories,” *Nuclear*

- Physics B **492**, 455 – 471 (1997).
- [57] U.-J. Wiese, “Ultracold quantum gases and lattice systems: quantum simulation of lattice gauge theories,” *Annalen der Physik* **525**, 777–796 (2013).
- [58] V Kasper, F Hebenstreit, F Jendrzejewski, M K Oberthaler, and J Berges, “Implementing quantum electrodynamics with ultracold atomic systems,” *New Journal of Physics* **19**, 023030 (2017).
- [59] Guo-Xian Su, Hui Sun, Ana Hudomal, Jean-Yves Desaulles, Zhao-Yu Zhou, Bing Yang, Jad C. Halimeh, Zhen-Sheng Yuan, Zlatko Papić, and Jian-Wei Pan, “Observation of unconventional many-body scarring in a quantum simulator,” arXiv e-prints (2022), [arXiv:2201.00821](https://arxiv.org/abs/2201.00821) [[cond-mat.quant-gas](https://arxiv.org/abs/2201.00821)].
- [60] Ana Hudomal, Jean-Yves Desaulles, Bhaskar Mukherjee, Guo-Xian Su, Jad C. Halimeh, and Zlatko Papić, “Driving quantum many-body scars in the PXP model,” *Phys. Rev. B* **106**, 104302 (2022).
- [61] Debasish Banerjee and Arnab Sen, “Quantum scars from zero modes in an abelian lattice gauge theory on ladders,” *Phys. Rev. Lett.* **126**, 220601 (2021).
- [62] Jean-Yves Desaulles, Debasish Banerjee, Ana Hudomal, Zlatko Papić, Arnab Sen, and Jad C. Halimeh, “Weak Ergodicity Breaking in the Schwinger Model,” arXiv e-prints (2022), [arXiv:2203.08830](https://arxiv.org/abs/2203.08830) [[cond-mat.str-el](https://arxiv.org/abs/2203.08830)].
- [63] Jean-Yves Desaulles, Ana Hudomal, Debasish Banerjee, Arnab Sen, Zlatko Papić, and Jad C. Halimeh, “Prominent quantum many-body scars in a truncated Schwinger model,” arXiv e-prints (2022), [arXiv:2204.01745](https://arxiv.org/abs/2204.01745) [[cond-mat.quant-gas](https://arxiv.org/abs/2204.01745)].
- [64] Sanjay Moudgalya and Olexei I. Motrunich, “Hilbert space fragmentation and commutant algebras,” *Phys. Rev. X* **12**, 011050 (2022).
- [65] Tibor Rakovszky, Pablo Sala, Ruben Verresen, Michael Knap, and Frank Pollmann, “Statistical localization: From strong fragmentation to strong edge modes,” *Phys. Rev. B* **101**, 125126 (2020).
- [66] Giuseppe De Tomasi, Daniel Hetterich, Pablo Sala, and Frank Pollmann, “Dynamics of strongly interacting systems: From fock-space fragmentation to many-body localization,” *Phys. Rev. B* **100**, 214313 (2019).
- [67] Zhi-Cheng Yang, Fangli Liu, Alexey V. Gorshkov, and Thomas Iadecola, “Hilbert-space fragmentation from strict confinement,” *Phys. Rev. Lett.* **124**, 207602 (2020).
- [68] I-Chi Chen and Thomas Iadecola, “Emergent symmetries and slow quantum dynamics in a rydberg-atom chain with confinement,” *Phys. Rev. B* **103**, 214304 (2021).
- [69] Sebastian Scherg, Thomas Kohlert, Pablo Sala, Frank Pollmann, Bharath Hebbe Madhusudhana, Immanuel Bloch, and Monika Aidelsburger, “Observing non-ergodicity due to kinetic constraints in tilted fermi-hubbard chains,” *Nature Communications* **12**, 4490 (2021).
- [70] Thomas Kohlert, Sebastian Scherg, Pablo Sala, Frank Pollmann, Bharath Hebbe Madhusudhana, Immanuel Bloch, and Monika Aidelsburger, “Exploring the regime of fragmentation in strongly tilted fermi-hubbard chains,” *Phys. Rev. Lett.* **130**, 010201 (2023).
- [71] Ulrich Schollwöck, “The density-matrix renormalization group in the age of matrix product states,” *Annals of Physics* **326**, 96–192 (2011), january 2011 Special Issue.
- [72] Sebastian Paecckel, Thomas Köhler, Andreas Swo-boda, Salvatore R. Manmana, Ulrich Schollwöck, and Claudius Hubig, “Time-evolution methods for matrix-product states,” *Annals of Physics* **411**, 167998 (2019).
- [73] See the Supplemental Material for additional analysis and background calculations to support the results in the main text. The supplementary material contains Refs. [68, 82, 85, 87–90].
- [74] Dayou Yang, Gouri Shankar Giri, Michael Johanning, Christof Wunderlich, Peter Zoller, and Philipp Hauke, “Analog quantum simulation of (1+1)-dimensional lattice QED with trapped ions,” *Phys. Rev. A* **94**, 052321 (2016).
- [75] E. Rico, T. Pichler, M. Dalmonte, P. Zoller, and S. Montangero, “Tensor networks for lattice gauge theories and atomic quantum simulation,” *Phys. Rev. Lett.* **112**, 201601 (2014).
- [76] Maarten Van Damme, Jad C. Halimeh, and Philipp Hauke, “Gauge-symmetry violation quantum phase transition in lattice gauge theories,” arXiv e-prints (2020), [arXiv:2010.07338](https://arxiv.org/abs/2010.07338) [[cond-mat.quant-gas](https://arxiv.org/abs/2010.07338)].
- [77] Sidney Coleman, R Jackiw, and Leonard Susskind, “Charge shielding and quark confinement in the massive Schwinger model,” *Annals of Physics* **93**, 267–275 (1975).
- [78] Soonwon Choi, Christopher J. Turner, Hannes Pichler, Wen Wei Ho, Alexios A. Michailidis, Zlatko Papić, Maksym Serbyn, Mikhail D. Lukin, and Dmitry A. Abanin, “Emergent SU(2) dynamics and perfect quantum many-body scars,” *Phys. Rev. Lett.* **122**, 220603 (2019).
- [79] Kieran Bull, Jean-Yves Desaulles, and Zlatko Papić, “Quantum scars as embeddings of weakly broken Lie algebra representations,” *Phys. Rev. B* **101**, 165139 (2020).
- [80] Thomas Iadecola, Michael Schecter, and Shenglong Xu, “Quantum many-body scars from magnon condensation,” *Phys. Rev. B* **100**, 184312 (2019).
- [81] Keita Omiya and Markus Müller, “Nature of many-body scars in a Rydberg chain: Gutzwiller projection of a large precessing pseudospin,” arXiv e-prints (2022), [arXiv:2203.00658](https://arxiv.org/abs/2203.00658) [[quant-ph](https://arxiv.org/abs/2203.00658)].
- [82] Paul Fendley, Bernard Nienhuis, and Kareljan Schoutens, “Lattice fermion models with supersymmetry,” *Journal of Physics A: Mathematical and General* **36**, 12399 (2003).
- [83] Haifeng Lang, Philipp Hauke, Johannes Knolle, Fabian Grusdt, and Jad C. Halimeh, “Disorder-free localization with Stark gauge protection,” arXiv e-prints (2022), [arXiv:2203.01338](https://arxiv.org/abs/2203.01338) [[cond-mat.quant-gas](https://arxiv.org/abs/2203.01338)].
- [84] Jad C. Halimeh, Haifeng Lang, Julius Mildenerger, Zhang Jiang, and Philipp Hauke, “Gauge-symmetry protection using single-body terms,” *PRX Quantum* **2**, 040311 (2021).
- [85] Johannes Hauschild and Frank Pollmann, “Efficient numerical simulations with Tensor Networks: Tensor Network Python (TeNPy),” *SciPost Phys. Lect. Notes* , 5 (2018), code available from <https://github.com/tenpy/tenpy>.
- [86] Adith Sai Aramthottil, Utso Bhattacharya, Daniel González-Cuadra, Maciej Lewenstein, Luca Barbiero, and Jakub Zakrzewski, “Scar states in deconfined z_2 lattice gauge theories,” *Phys. Rev. B* **106**, L041101 (2022).
- [87] C. J. Turner, J.-Y. Desaulles, K. Bull, and Z. Papić, “Correspondence principle for many-body scars in ultracold rydberg atoms,” *Phys. Rev. X* **11**, 021021 (2021).
- [88] Sergey Bravyi, David P. DiVincenzo, and Daniel Loss, “Schrieffer–wolf transformation for quantum many-body systems,” *Annals of Physics* **326**, 2793 – 2826 (2011).
- [89] Wen Wei Ho, Soonwon Choi, Hannes Pichler, and Mikhail D. Lukin, “Periodic orbits, entanglement, and

quantum many-body scars in constrained models: Matrix product state approach,” *Phys. Rev. Lett.* **122**, 040603 (2019).

- [90] A. A. Michailidis, C. J. Turner, Z. Papić, D. A. Abanin, and M. Serbyn, “Slow quantum thermalization and many-body revivals from mixed phase space,” *Phys. Rev. X* **10**, 011055 (2020).

— Supplemental Material —

Ergodicity Breaking Under Confinement in Cold-Atom Quantum Simulators

Jean-Yves Desaulès, Guo-Xian Su, Ian P. McCulloch, Bing Yang, Zlatko Papić, and Jad C. Halimeh

In this Supplementary Material, we provide additional analysis and background calculations to support the results in the main text. In Sec. D, we provide additional details on scarring from the Néel state at low values of χ . In Sec. E, we discuss the particle-hole symmetry of the system when $\mu = 0$ and its consequences. In Sec. F, we show the derivation of the effective Hamiltonians in the non-ergodic regimes using a Schrieffer-Wolf transformation. In Sec. G, we provide additional details about the MPS computation for the spreading of defects in the PXP model. In Sec. H, we show that the non-monotonicity of the revivals from the Néel state as χ is increased can also be seen in the semi-classical limit using TDVP.

Appendix D: Additional results on scarring from the Néel state with $\mu = 0$

In this section we provide additional results on quenches from the Néel state with $\mu = 0$. Fig. S1 shows

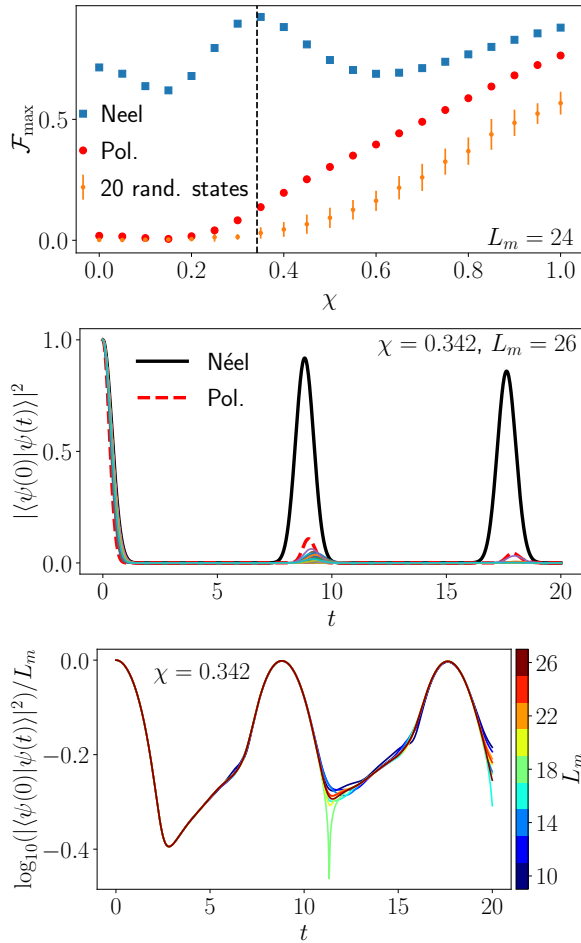


FIG. S1. (Color online). Top: fidelity at the first revival from various product states with $\chi = 0.342$ and $L_m = 24$. Middle: fidelity dynamics after quenches from various product states with $\chi = 0.342$ and $L_m = 26$. Bottom: fidelity after quenches from the Néel state $\chi = 0.342$ and various system sizes.

that the non-monotonic fidelity behavior witnessed for

this state is not visible when quenching from other initial product states. It also shows that at $\chi = 0.342$, close to

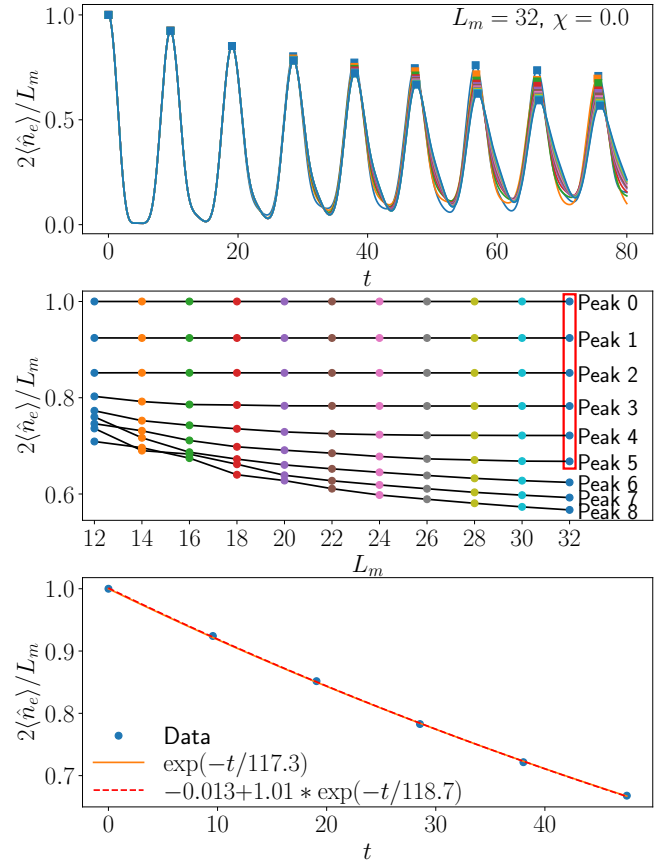


FIG. S2. (Color online). Occupation density on the even sublattice after quenches from the Néel state for $\chi = 0$ and various system sizes. Top: data for all system sizes. The square indicate the local maxima. Middle: Local maxima as a function of system size. Each line correspond to a different peak and each color to a different system size. The red rectangle highlights the peaks that are converged in system size at $L_m = 32$ and that will be used to extract a decay timescale. Bottom: Exponential fit of the converged peaks for $L_m = 32$ to get the decay exponent of the envelope.

the optimal point for the Néel state, other states display relatively quick thermalization in large systems. Finally, the bottom panel of the same figure shows that after

quenches from the Néel state the fidelity density is well converged already at small system sizes $L_m \approx 14$. All these results confirm that the revivals witnessed around $\chi = 0.342$ for the Néel state are genuine scarring and are not due to fragmentation or to finite-size effects.

We now show more details on how Fig. 3(b) in the main text is obtained. We perform quenches from the Néel state and monitor the excitation density on the even sublattice. We do this for several system sizes and identify the local maxima for each of them. We can then see which of these are converged in system size and discard the other ones. We finally fit these maxima with a decaying exponential of the form $f(t) = a + be^{-t/\tau}$. Fig. S2 shows the raw data for various system sizes, the scaling of the height of each peak with system sizes, and finally the plot of the converged peaks for $\chi = 0$. We reproduce the same procedure for $\chi = 0.15$, $\chi = 0.3$ and $\chi = 0.6$. For brevity we do not show the full data here but only the converged peaks and their exponential fit (see Fig. 3(b) in the main text). We note that as χ gets larger the finite-size effects seem to occur at increasingly longer times. Overall we find a clear difference between $\chi = 0.3$ and the other values already after 3-4 revivals. The decay time τ also shows a much larger value around $\chi = 0.3$.

Appendix E: Particle-hole symmetry with $\chi \neq 0$

In the PXP model with an even system size, the Néel state $|\mathbf{Z}_2\rangle$ and anti-Néel state $|\overline{\mathbf{Z}}_2\rangle$ are degenerate for any value of μ as long as $\chi = 0$. A non-zero value of χ will break that as one of the state goes towards the ground state and the other one towards the sky state. Nonetheless, when $\mu = 0$ they still show identical dynamics for any χ due to the symmetry of the spectrum. Let us start with the PXP model with $\mu = 0$ and an even number of sites $L_m = 2M$ and rewrite it as

$$\hat{H}_{PXP} = \hat{H}_0 + \hat{H}_\chi \quad (\text{S1})$$

For $\mu = \chi = 0$, it is well known that the spectrum has a particle-hole symmetry with respect to the operator

$$\hat{\mathcal{Z}} = \prod_{j=1}^{L_m} \hat{s}_j^z \quad (\text{S2})$$

as $\{\hat{H}_0, \hat{\mathcal{Z}}\} = 0$. At the same time, the Hamiltonian is also symmetric under the spatial inversion operator $\hat{\mathcal{L}}$ that takes site j to $L_m + 1 - j$ and so $[\hat{H}_0, \hat{\mathcal{L}}] = 0$. Interestingly, the staggered potential term \hat{H}_χ has the exact inverse relations with these two operators and $[\hat{H}_\chi, \hat{\mathcal{Z}}] = 0$, while $\{\hat{H}_\chi, \hat{\mathcal{L}}\} = 0$. Both these operators are hermitian and have a square equal to the identity $\hat{\mathcal{L}}^2 = \hat{\mathcal{Z}}^2 = \mathbb{1}$. They also commute with each other.

It is then straightforward to prove that $\hat{H}_0 + \hat{H}_\chi$ anti-commutes with $\hat{\mathcal{L}}\hat{\mathcal{Z}}$. Indeed, we have that

$$\begin{aligned} (\hat{H}_0 + \hat{H}_\chi) \hat{\mathcal{L}}\hat{\mathcal{Z}} &= \hat{\mathcal{L}} (\hat{H}_0 - \hat{H}_\chi) \hat{\mathcal{Z}} \\ &= \hat{\mathcal{L}}\hat{\mathcal{Z}} (-\hat{H}_0 - \hat{H}_\chi) \\ &= -\hat{\mathcal{L}}\hat{\mathcal{Z}} (\hat{H}_0 + \hat{H}_\chi). \end{aligned} \quad (\text{S3})$$

This has a few direct consequences, such as the presence of the same number of zero-modes as for $\chi = 0$ and the fact that the spectrum is symmetric around $E = 0$.

It also has less obvious consequences for the Néel and anti-Néel states, as both $\hat{\mathcal{L}}$ and $\hat{\mathcal{Z}}$ have special relations these two states. They are eigenstates of $\hat{\mathcal{Z}}$ with eigenvalue $(-1)^M$, while $\hat{\mathcal{L}}$ takes one to the other as $|\overline{\mathbf{Z}}_2\rangle = \hat{\mathcal{L}}|\mathbf{Z}_2\rangle$. These properties allow us to directly show that for any value of χ , the return fidelity of both states will be exactly identical as long as μ is 0. Let us first consider the energy expectation value of both states:

$$\begin{aligned} \langle \overline{\mathbf{Z}}_2 | \hat{H}_{PXP} | \overline{\mathbf{Z}}_2 \rangle &= \langle \mathbf{Z}_2 | \hat{\mathcal{L}} (\hat{H}_0 + \hat{H}_\chi) \hat{\mathcal{L}} | \mathbf{Z}_2 \rangle \\ &= \langle \mathbf{Z}_2 | (\hat{H}_0 - \hat{H}_\chi) \hat{\mathcal{L}} \hat{\mathcal{L}} | \mathbf{Z}_2 \rangle \\ &= \langle \mathbf{Z}_2 | \hat{\mathcal{Z}} \hat{\mathcal{Z}} (\hat{H}_0 - \hat{H}_\chi) | \mathbf{Z}_2 \rangle \\ &= \langle \mathbf{Z}_2 | \hat{\mathcal{Z}} (-\hat{H}_0 - \hat{H}_\chi) \hat{\mathcal{Z}} | \mathbf{Z}_2 \rangle \\ &= (-1)^{2M+1} \langle \mathbf{Z}_2 | (\hat{H}_0 + \hat{H}_\chi) | \mathbf{Z}_2 \rangle \\ &= -\langle \mathbf{Z}_2 | \hat{H}_{PXP} | \mathbf{Z}_2 \rangle. \end{aligned} \quad (\text{S4})$$

We indeed find that the degeneracy between them is broken. The exact same procedure can be done for any arbitrary power of the Hamiltonian to get

$$\langle \overline{\mathbf{Z}}_2 | \hat{H}_{PXP}^k | \overline{\mathbf{Z}}_2 \rangle = (-1)^k \langle \mathbf{Z}_2 | \hat{H}_{PXP}^k | \mathbf{Z}_2 \rangle. \quad (\text{S5})$$

This allows us to easily compute the return fidelity by doing the power expansion of the exponential of the Hamiltonian as

$$\begin{aligned} \langle \overline{\mathbf{Z}}_2 | e^{-it\hat{H}_{PXP}} | \overline{\mathbf{Z}}_2 \rangle &= \sum_{k=0}^{\infty} (-it)^k \langle \overline{\mathbf{Z}}_2 | \hat{H}_{PXP}^k | \overline{\mathbf{Z}}_2 \rangle \\ &= \sum_{k=0}^{\infty} (it)^k \langle \mathbf{Z}_2 | \hat{H}_{PXP}^k | \mathbf{Z}_2 \rangle \\ &= \langle \mathbf{Z}_2 | e^{it\hat{H}_{PXP}} | \mathbf{Z}_2 \rangle \\ &= \left(\langle \mathbf{Z}_2 | e^{-it\hat{H}_{PXP}} | \mathbf{Z}_2 \rangle \right)^* \end{aligned} \quad (\text{S6})$$

From there it is trivial to see that

$$|\langle \overline{\mathbf{Z}}_2 | e^{-it\hat{H}_{PXP}} | \overline{\mathbf{Z}}_2 \rangle|^2 = |\langle \mathbf{Z}_2 | e^{-it\hat{H}_{PXP}} | \mathbf{Z}_2 \rangle|^2 \quad (\text{S7})$$

Similar equivalences can be proven for the expectation of an operator \hat{O} after quenches from the Néel and anti-Néel states as long as $[\hat{O}, \hat{\mathcal{L}}\hat{\mathcal{Z}}] = 0$. So while the spatial symmetries of the Hamiltonian do not guarantee any

equivalence between the Néel and anti-Néel states after a quenches, the particle-hole symmetry actually does.

This immediately breaks down when a non-zero μ is added. The simplest way to see this is by checking the relation between the chemical potential term \hat{H}_μ and $\hat{\mathcal{L}}$ and $\hat{\mathcal{Z}}$. A quick calculation yields $[\hat{H}_\mu, \hat{\mathcal{L}}] = [\hat{H}_\mu, \hat{\mathcal{Z}}] = 0$. So in the procedure used in this section neither $\hat{\mathcal{L}}$ nor $\hat{\mathcal{Z}}$ can be used to change the sign of \hat{H}_μ and it will not be possible to get a term equal to $-\hat{H}_{PXP}$.

Appendix F: $|\mu|, |\chi| \gg \kappa$ limit in the PXP model

In the limit where the mass and confining potential are much larger than the hopping term κ , the Hilbert space fractures and we can perform a Schrieffer-Wolf (SW) transformation [S1] by writing the PXP Hamiltonian as $\hat{H}_0 + \kappa\hat{V}$ with

$$\hat{H}_0 = -\sum_{l=1}^{L_m} [2\mu + (-1)^l \chi] \hat{s}_l^z, \quad \hat{V} = -\sum_{l=1}^{L_m} \hat{P}_{l-1} \hat{s}_l^x \hat{P}_{l+1}. \quad (\text{S1})$$

Each sector is characterized by a different expectation value of H_0 , which we will denote by d_0 . As this operator is diagonal in the Fock basis, it is convenient to express each subspace as the span of all Fock states $|\psi\rangle$ with $\langle\psi|H_0|\psi\rangle = d_0$. Let us denote the number of excitations on the odd (even) sublattice by $n_o(n_e)$. Let us also assume an even number of sites $L_m = 2M$, so we have M sites on each sublattice. Adding an excitation on an odd site lead to an energy change of $-2\mu + \chi$, and on an even site to an energy change of $-2\mu - \chi$. We can finally write

$$d_0 = (n_o - \frac{M}{2})(-2\mu + \chi) + (n_e - \frac{M}{2})(-2\mu - \chi). \quad (\text{S2})$$

In order to perform the SW transformation, we can follow the same procedure as in Ref. [S2] in which the case $\mu = 0$ was investigated. We first need to find the Schrieffer-Wolf generator $\hat{S}^{(1)}$ that obeys

$$[\hat{S}^{(1)}, \hat{H}_0] + \hat{V} = 0. \quad (\text{S3})$$

This is straightforward to do and leads to

$$\hat{S}^{(1)} = i \sum_{j=1}^{L_m} \frac{\hat{P}_{j-1} \hat{s}_j^y \hat{P}_{j+1}}{2\mu + (-1)^j \chi}, \quad (\text{S4})$$

which is well defined as long as $\chi \neq \pm 2\mu$. The case $\chi = \pm 2\mu$ will be treated separately in the next section, and for now we assume $\chi \neq \pm 2\mu$. The effective Hamiltonian at order n can then be computed as

$$\hat{H}_{\text{eff}}^{(n)} = \kappa^n \frac{n-1}{n!} \hat{\mathcal{P}}_0 \underbrace{[\hat{S}^{(1)}, [\hat{S}^{(1)}, \dots, [\hat{S}^{(1)}, \hat{V}] \dots]]}_{n-1} \hat{\mathcal{P}}_0 \quad (\text{S5})$$

for $n > 1$, where $\hat{\mathcal{P}}_0$ is the projector that project each term into sectors with fixed d_0 . The first order Hamiltonian can also be directly computed as

$$\hat{H}_{\text{eff}}^{(1)} = \kappa \hat{\mathcal{P}}_0 \hat{V} \hat{\mathcal{P}}_0. \quad (\text{S6})$$

However, as \hat{V} has no term that conserves d_0 , $\hat{H}_{\text{eff}}^{(1)}$ is identically zero. This is also true for all odd order terms.

To compute the effective Hamiltonian up to 4th order we need to compute

$$\begin{aligned} [\hat{S}^{(1)}, \hat{V}] = & -\sum_{j=1}^{L_m} \frac{\hat{P}_{j-1} \hat{s}_j^z \hat{P}_{j+1}}{2\mu + (-1)^j \chi} \\ & -\mu \sum_{j=1}^{L_m} \frac{\hat{P}_{j-1} \hat{\sigma}_j^+ \hat{\sigma}_{j+1}^- \hat{P}_{j+2} + \hat{P}_{j-1} \hat{\sigma}_j^- \hat{\sigma}_{j+1}^+ \hat{P}_{j+2}}{4\mu^2 - \chi^2}, \end{aligned} \quad (\text{S7})$$

$$\begin{aligned} [\hat{S}^{(1)}, [\hat{S}^{(1)}, \hat{V}]] = & -\sum_{j=1}^{L_m} \frac{\hat{P}_{j-1} \hat{s}_j^x \hat{P}_{j+1}}{(2\mu + (-1)^j \chi)^2} \\ & + \sum_{j=1}^{L_m} \frac{2\mu + 1}{(2\mu - (-1)^j \chi)} \frac{\hat{P}_{j-2} \hat{P}_{j-1} \hat{s}_j^x \hat{P}_{j+1} + \hat{P}_{j-1} \hat{s}_j^x \hat{P}_{j+1} \hat{P}_{j+2}}{2(4\mu^2 - \chi^2)} \\ & - \mu \sum_{j=1}^{L_m} \frac{\hat{P}_{j-2} \hat{\sigma}_{j-1}^+ \hat{\sigma}_j^- \hat{\sigma}_{j+1}^+ \hat{P}_{j+2} + \text{h.c.}}{(4\mu^2 - \chi^2)(2\mu - (-1)^j \chi)}, \end{aligned} \quad (\text{S8})$$

and finally

$$\begin{aligned} [\hat{S}^{(1)}, [\hat{S}^{(1)}, [\hat{S}^{(1)}, \hat{V}]]] = & \sum_{j=1}^{L_m} \frac{\hat{P}_{j-1} \hat{s}_j^z \hat{P}_{j+1}}{(2\mu + (-1)^j \chi)^3} \\ & + \frac{4\mu - (-1)^j \chi}{2(4\mu^2 - \chi^2)^2} \left(\hat{P}_{j-2} \hat{P}_{j-1} \hat{s}_j^z \hat{P}_{j+1} + \hat{P}_{j-1} \hat{s}_j^z \hat{P}_{j+1} \hat{P}_{j+2} \right) \\ & + \frac{4\mu + (-1)^j \chi}{4(4\mu^2 - \chi^2)^2} \left(\hat{P}_{j-2} \hat{\sigma}_{j-1}^+ \hat{P}_j \hat{\sigma}_{j+1}^- \hat{P}_{j+2} + \text{h.c.} \right) \\ & + \frac{6\mu + (-1)^j \chi}{4(4\mu^2 - \chi^2)^2} \left(\hat{P}_{j-2} \hat{\sigma}_{j-1}^+ \hat{P}_j \hat{\sigma}_{j+1}^+ \hat{P}_{j+2} + \text{h.c.} \right) \\ & - \frac{\mu}{(4\mu^2 - \chi^2)^2} \left(\hat{P}_{j-1} \hat{\sigma}_j^+ \hat{\sigma}_{j+1}^- \hat{\sigma}_{j+2}^+ \hat{\sigma}_{j+3}^- \hat{P}_{j+4} + \text{h.c.} \right) \\ & + \mu \frac{8\mu^2 - \chi^2}{(4\mu^2 - \chi^2)^3} \left(\hat{P}_{j-1} \hat{\sigma}_j^+ \hat{\sigma}_{j+1}^- \hat{P}_{j+2} + \text{h.c.} \right) \\ & + \frac{(8\mu + (-1)^j \chi) \left(\hat{P}_{j-1} \hat{\sigma}_j^+ \hat{\sigma}_{j+1}^- \hat{P}_{j+2} \hat{P}_{j+3} + \text{h.c.} \right)}{8(2\mu + (-1)^j \chi)^2 (4\mu^2 - \chi^2)} \\ & + \frac{(8\mu - (-1)^j \chi) \left(\hat{P}_{j-2} \hat{P}_{j-1} \hat{\sigma}_j^+ \hat{\sigma}_{j+1}^- \hat{P}_{j+2} + \text{h.c.} \right)}{8(2\mu - (-1)^j \chi)^2 (4\mu^2 - \chi^2)}. \end{aligned} \quad (\text{S9})$$

1. General case, μ/χ irrational

If χ/μ is irrational, each sector is characterized by the number of excitations on each sublattice, n_o and n_e . Us-

ing Eq. (S4), it is straightforward to derive the next order terms in the SW transformation. The leading order is then the second order one which is diagonal, giving

$$\hat{H}_{\text{eff}}^{(2)} = -\frac{\kappa^2}{2} \sum_{j=1}^{L_m} \frac{\hat{P}_{j-1} \hat{s}_j^z \hat{P}_{j+1}}{2\mu + (-1)^j \chi}. \quad (\text{S10})$$

The next non-zero term is at 4th order and reads

$$\begin{aligned} \hat{H}^{(4)} &= \frac{\kappa^4}{32} \sum_{j=1}^{L_m} 4 \frac{\hat{P}_{j-1} \hat{s}_j^z \hat{P}_{j+1}}{(2\mu + (-1)^j \chi)^3} \\ &+ 2 \frac{4\mu - (-1)^j \chi}{(4\mu^2 - \chi^2)^2} \left(\hat{P}_{j-2} \hat{P}_{j-1} \hat{s}_j^z \hat{P}_{j+1} + \hat{P}_{j-1} \hat{s}_j^z \hat{P}_{j+1} \hat{P}_{j+2} \right) \\ &+ \frac{4\mu + (-1)^j \chi}{(4\mu^2 - \chi^2)^2} \left(\hat{P}_{j-2} \hat{s}_{j-1}^+ \hat{P}_j \hat{s}_{j+1}^- \hat{P}_{j+2} + \text{h.c.} \right). \end{aligned} \quad (\text{S11})$$

These terms are all similar to the ones studied in Ref. [S2] for $\mu = 0$, and match them exactly at that point. As the off-diagonal terms are the same (up to an overall factor), the connectivity of the Hilbert space is the same up to that point. So we will not focus more on this case as it has already been studied extensively.

Instead we will show that adding the mass term μ allows to engineer different types of fragmentation due to resonances between the χ and μ term.

2. Resonances

There is technically an infinite number of resonances between μ and χ . The simplest case in which they happen is when the energy difference on one sublattice is equal to n times the energy change on the other with n integer. Hence two configurations can have a different number of excitations on their sublattices but still the same d_0 . The resonance condition can be expressed as

$$2\mu \pm \chi = n(2\mu \mp \chi) \rightarrow \mu = \pm \frac{n+1}{2(n-1)} \chi, \quad (\text{S12})$$

and setting these values can lead to a resonance at order $|n| + 1$ at the minimum. Indeed, the allowed processes that match the resonance require to add n excitations on one sublattice and remove one on the other, so they require $n + 1$ moves. We can also choose n to be a negative integer. In that case we need to do the same operation (add or remove) on both sublattices. In general, as we have a dynamical term at 4th order for any value of μ and χ , anything beyond $|n| = 3$ will never be the dominant off-diagonal term.

More complex resonances can also occur, in which the ratio between the energy cost of an excitation on each sublattice is not an integer but a rational number. In this case we have the same condition as in Eq. S12 but with n a rational number. Let us denote by a and b the numerator and denominator of the irreducible form of n .

In that case the resonance can only lead to new terms in the effective Hamiltonian at order $a + b$.

As integers can be represented with $b = 1$, this matches in the limit of n integers. Let us also note that taking a fraction with $a = 1$ will lead to the same result as the integer case with $n = -b$. With that in mind, the simplest case that does not fit in the integer limit is $a = 2$ and $b = 3$ or vice-versa. As this can only lead to new effective terms at order 5 or more, we will not consider these and focus on integer n .

$$a. \quad n = 0: \quad \chi = \pm 2\mu$$

For that particular relation between the two parameters, we have that μ and χ add up on one sublattice and cancel on the other one. For brevity we will discuss the case $\chi = -2\mu$, for which $d_0 = 2\chi(n_o - \frac{M}{2})$. Here we see that the fragments are much larger than in the trivial case.

The approach used to compute the SW transformation terms in Eq. S5 fails as \hat{V} now has terms within individual sectors. This results in an operator $\hat{S}^{(1)}$ with some infinite matrix elements (see Eq. S4). However it also means that the first order effective Hamiltonian – Eq. (S6) – is non-zero. It is the leading order Hamiltonian and is given by

$$\hat{H}_{\text{eff}}^{(1)} = -\kappa \sum_{j=0}^M \hat{P}_{2j-1} \hat{s}_{2j}^x \hat{P}_{2j+1} \quad (\text{S13})$$

So all the odd sites are frozen while the even one can flip freely if their neighbours are frozen in the unexcited position.

As the odd sites are frozen, two configurations with the same n_o but different arrangements of them will be disconnected. So in each sector with a fixed d_0 , the Hilbert space shows further fragmentation. The number of subsectors is given by the number of unique configurations on the odd sites, hence it is

$$\mathcal{N}_{n_o} = \binom{L_m/2}{n_o}. \quad (\text{S14})$$

The size of each sector is then 2^k , where k denotes the number of even sites with unexcited neighbors. This is not uniquely determined by L_m and n_o , as even with these two parameters fixed different configurations on the odd sites can lead to different values k .

Note that all sites are either completely frozen (odd sites and the neighbours of excited odd sites) or allowed to flip freely without any interaction (even sites with both neighbours frozen in the unexcited positions). So the effective model at first order is that of a free paramagnet. Let us denote by \mathcal{K} the set of all non-frozen (even) sites, then we can recast the Hamiltonian as

$$\hat{H}^{(1)} = -\kappa \sum_{j \in \mathcal{K}} \hat{s}_j^x. \quad (\text{S15})$$

The same transformation can be done in the vicinity of the resonance $\chi = -2\mu + \gamma$ as long as γ is not much larger than κ . The expression of d_0 becomes $d_0 = (2\chi - \gamma)(n_o - \frac{M}{2})$ and the odd sites are still frozen, but now the first order Hamiltonian gains a diagonal contribution as

$$\hat{H}^{(1)} = -\kappa \sum_{j \in \mathcal{K}} \hat{s}_j^x - \sum_{j=0}^M \gamma \hat{s}_{2j}^z = E_0 - \sum_{j \in \mathcal{K}} \kappa \hat{s}_j^x + \gamma \hat{s}_j^z, \quad (\text{S16})$$

where E_0 is the (constant) contribution of all frozen even sites. This Hamiltonian is still integrable, but the energy of the eigenstates and the revival period from the Fock states is altered.

If $\chi = +2\mu$, the same analysis can be done but the even sites are frozen and the odd ones can flip freely if their neighbours are down.

$$b. \quad n = 1: \chi = 0$$

If $n = 1$, we get $\mu = \pm\infty\chi$, meaning that μ can take any value but that χ must be 0. That regime is quite special, as it does not have confinement and the only thing slowing down the dynamics is the large mass of the fermionic matter. Nonetheless we can treat it like the non-resonant case, and we find that $d_0 = 2\mu(n_o + n_e - M)$. The $\hat{S}^{(1)}$ operator and its commutators with respect to \hat{V} are the same, but the projector \hat{P}_0 is changed to reflect the new d_0 . It now leaves $\hat{P}_{j-1}\hat{\sigma}_j^+\hat{\sigma}_{j+1}^-\hat{P}_{j+2}$ unaffected as even and odd sites are on an equal footing. So moving an excitation between neighbours preserves d_0 , which only depends on the total number of excitations, and there is an emergent $U(1)$ symmetry. The effective Hamiltonian at 2nd order is then

$$\hat{H}_{\text{eff}}^{(2)} = -\frac{\kappa^2}{8\mu} \sum_{j=1}^{L_m} \left(2\hat{P}_{j-1}\hat{s}_j^z\hat{P}_{j+1} + \hat{P}_{j-1}\hat{\sigma}_j^+\hat{\sigma}_{j+1}^-\hat{P}_{j+2} + \text{h.c.} \right). \quad (\text{S17})$$

We note that in this regime there is no Hilbert space fragmentation. Indeed, in each $U(1)$ sector all states are connected.

What is interesting to note is that this effective Hamiltonian resembles the lattice fermions \mathcal{M}_1 supersymmetric model introduced in Ref. [S3]. The two terms that compose the Hamiltonian are the same, but their prefactors are different. The same mapping to the XXZ model can be done, albeit with a different value of Δ . Consequently, in each of the $U(1)$ sectors the effective Hamiltonian is integrable.

We can also study what happens if we add a small χ such that $\kappa, \chi \ll \mu$. In this case we have

$$\hat{H}_0 = -\sum_{l=1}^{L_m} 2\mu \hat{s}_l^z, \quad \hat{V} = -\sum_{l=1}^{L_m} \left[\hat{P}_{l-1} \hat{s}_l^x \hat{P}_{l+1} + (-1)^l \frac{\chi}{\kappa} \hat{s}_l^z \right]. \quad (\text{S18})$$

The PXP term will lead to the same 2nd order term, while the $(-1)^l \hat{s}_l^z$ term will add a first order term. We end up with

$$\hat{H}_{\text{eff}}^{(1,2)} = -\frac{\kappa^2}{8\mu} \sum_{j=1}^{L_m} \left(2\hat{P}_{j-1}\hat{s}_j^z\hat{P}_{j+1} + \hat{P}_{j-1}\hat{\sigma}_j^+\hat{\sigma}_{j+1}^-\hat{P}_{j+2} + \text{h.c.} \right) - \sum_{j=1}^{L_m} (-1)^j \chi \hat{s}_j^z \quad (\text{S19})$$

This Hamiltonian no longer maps to the XXZ model, and when χ and $\frac{\kappa^2}{8\mu}$ are of comparable strength we find level spacing statistics close to Wigner-Dyson.

$$c. \quad n = 2: \mu = \pm\frac{3}{2}\chi$$

For $n = 2$, we have $\mu = \pm\frac{3}{2}\chi$. The sign just changes which sublattice is affected, so we will only focus on the case $\mu = \frac{3}{2}\chi$. In that case,

$$d_0 = (-2\chi)(n_o + 2n_e - \frac{3}{2}M). \quad (\text{S20})$$

We then find that the effective 3rd order Hamiltonian is

$$\begin{aligned} \hat{H}_{\text{eff}}^{(3)} &= -\frac{\mu\kappa^3}{3} \sum_{j=1}^{L_m} \frac{\hat{P}_{2j-2}\hat{\sigma}_{2j-1}^+\hat{\sigma}_{2j}^-\hat{\sigma}_{2j+1}^+\hat{P}_{2j+2} + \text{h.c.}}{(4\mu^2 - \chi^2)(2\mu - (-1)^j\chi)} \\ &= -\frac{\kappa^3}{32\chi^2} \sum_{j=1}^M \hat{P}_{2j-2}\hat{\sigma}_{2j-1}^+\hat{\sigma}_{2j}^-\hat{\sigma}_{2j+1}^+\hat{P}_{2j+2} + \text{h.c.} \end{aligned} \quad (\text{S21})$$

This corresponds to projecting a term of the form $\hat{P}_{j-2}\hat{s}_{j-1}^x\hat{s}_j^x\hat{s}_{j+1}^x\hat{P}_{j+2}$ into the constrained Hilbert space of the PXP model. It is also important to keep in mind that even if this is the leading dynamical term, the diagonal Hamiltonian obtained at second order – see Eq. S10 – is still present here. The Hilbert space of the third order Hamiltonian is further fragmented. This can be seen by recognising that the configuration $\circ_{2j-4}\circ_{2j-3}\bullet_{2j-2}\circ_{2j-1}\bullet_{2j}\circ_{2j+1}\circ_{2j+2}$ is frozen. Indeed, the only term that can remove an excitation on an even site is dressed with projectors on the two neighbouring even sites. This effectively creates an equivalent of the PXP constraint between even sites. Every pair of excitations on consecutive even sites cannot be removed or created by the Hamiltonian in Eq. (S21).

The largest fragment is the one containing the state $|\mathbf{Z}'_4\rangle = |\circ\bullet\circ\circ\bullet\circ\circ\cdots\circ\bullet\circ\rangle$. This fragment can actually be mapped exactly onto the PXP model with $L_m/2$ sites. The mapping is relatively straightforward, as the PXP state simply corresponds to the configuration of the even sites. We recognise that the $|\mathbf{Z}'_4\rangle$ state is thus the Néel state. The odd sites still play a role at enforcing the effective PXP constraint. If there is an excitation on an even site, it is always possible to remove it as $\circ\bullet\circ \rightarrow \bullet\circ\bullet$. However, if there is no excitation on an even site, in order

to create one both neighbours must be excited in order to do the process $\bullet\bullet\bullet \rightarrow \circ\bullet\circ$. But excitations on the neighbouring odd sites are only created when deexciting the neighboring even sites. This means that an even site can only be excited if both of its even neighbors are not, exactly as expected from the PXP constraint. Here we provide a quick example correspond to going from $\bullet\bullet\bullet \rightarrow \circ\bullet\circ$ (in PXP terms):

$$\bullet\bullet\bullet\bullet\bullet\bullet \rightarrow \circ\bullet\bullet\bullet\bullet\bullet \rightarrow \bullet\circ\bullet\bullet\bullet\bullet \rightarrow \bullet\bullet\circ\bullet\bullet\bullet. \quad (\text{S22})$$

We stress that this effective PXP constraint is not simply a consequence of the emergent conserved quantity. Indeed, as shown in Eq. (S20) it only depends on the number of excitation on even and odd sites, and does not take into account their positions beyond that. So the emergent PXP constraint is a symptom of true Hilbert space fragmentation. It can be associated with a set of $L_m/2$ independent conserved quantities $\left\{ \hat{n}_{2j} \hat{n}_{2j+2} \right\}_{j=1}^{L_m}$.

We also note here that the leading order Hamiltonian is still the second order one in Eq. (S17). Furthermore, no process generated by Eq. (S21) preserves the expectation value of $\hat{H}_{\text{eff}}^{(2)}$. As such $\hat{H}_{\text{eff}}^{(3)}$ is further suppressed, and one would need to perform a nested Schrieffer-Wolf transformation with $\hat{H}_{\text{eff}}^{(2)}$ as \hat{H}_0 and $\hat{H}_{\text{eff}}^{(3)}$ as \hat{V} in order to get the right leading terms and prefactors.

$$d. \quad n = -1: \mu = 0$$

This resonance happens when $\mu = 0$, and has been treated extensively in Ref. [S2]. While it produces an effective Hamiltonian at 2nd order, this Hamiltonian is also purely diagonal. So there is no additional term due to this resonance. As removing (or adding) an excitation on both sublattices does not change d_0 , we could expect a term of the form $\hat{P}_{j-1} \hat{s}_j^+ \hat{s}_{j+1}^+ \hat{P}_{j+2} + \text{h.c.}$. However it is clear that such a term is forbidden by the PXP constraint. Any longer range term $\hat{P}_{j-1} \hat{s}_j^+ \hat{P}_{j+1} \hat{P}_{j+2r} \hat{s}_{j+2r+1}^+ \hat{P}_{j+2r+2} + \text{h.c.}$ with r integer is also identically zero. Indeed, both sites are far enough apart so that they do not interact through the constraint. As a consequence the order in which the excitations are added does not matter. But both possible paths have opposite signs, and so they exactly cancel each other. This is the same reason why there are generically no long-range processes in the effective Hamiltonians obtained for these models.

The same observation can be made for the 4th order Hamiltonian, as it does not contain any additional term when compared to the one in the incommensurate case.

$$e. \quad n = -2, n = -3 \text{ and } n = 3$$

As for $n = -1$, $n = -2$, $n = -3$ and $n = 3$ do not lead to additional terms in the effective Hamiltonian up to 4th

order. This can be seen in the expressions in Eqs. (S7)-S9, as none of the terms that get projected out by $\hat{\mathcal{P}}_0$ in the incommensurate case survive here. For $n = -2$, we would need terms with 2 \hat{s}^+ on one sublattice and one \hat{s}^+ on the other sublattice. For $n = -3$, we would need terms with 3 \hat{s}^+ on one sublattice and one \hat{s}^+ on the other sublattice. For $n = 3$, we would need terms with 3 \hat{s}^+ on one sublattice and one \hat{s}^- on the other sublattice. It is straightforward to see so none of these terms show up, and as such there is no meaningful difference with the incommensurate case up to 4th order.

3. Resonances at intermediate values of μ and χ

For values of χ and μ which are equal to only a few time κ , the system already starts to form fragments with a definite value of d_0 . However, they are still weakly connected and multiple of them contribute to the dynamics. At the resonances discussed, the sectors have an energy spacing that is always commensurate and so this can lead to revivals. This occurs for example for the Néel state around $\chi = 0.6$ and $\mu = -0.9$.

Appendix G: MPS methods

In order to reach large systems to assess confinement in the PXP model, we use matrix product state (MPS) techniques. More specifically, we use TDVP as implemented in the TeNPy package [S4]. We use two-site TDVP as first to grow the bond-dimension until it saturates to a desired value. At that point, we switch to one-site TDVP as it is faster and exactly conserves the energy. We also use OBC instead of PBC to avoid correlations spanning the whole length of the chain. The initial state chosen is then $\bullet\bullet\bullet\circ\cdots\circ\bullet$ as it leads to suppressed boundary effects. The results were compared to exact ones for 29 sites, and different bond-dimensions were used to assess convergence. Fig. S3 shows the data for the RMS ZZ correlator for two different bond-dimension, as well as their difference. The results in Fig. 5 in the main text can also be compared with their equivalent using exact time-evolution for $L_m = 32$ and PBC in Fig. S4. Times as long as 70 units cannot be reached as the particle and antiparticle have scattered with each other already at time ≈ 50 . Nonetheless, we qualitatively see the same as in the larger system with OBC. Not only do we see confinement, we also see the same synchronization of oscillations in the case with $\chi = 0.35$.

Appendix H: Symmetric subspace and TDVP semi-classical limit

Another approximation that allows to study the PXP model for even larger systems is the symmetric subspace

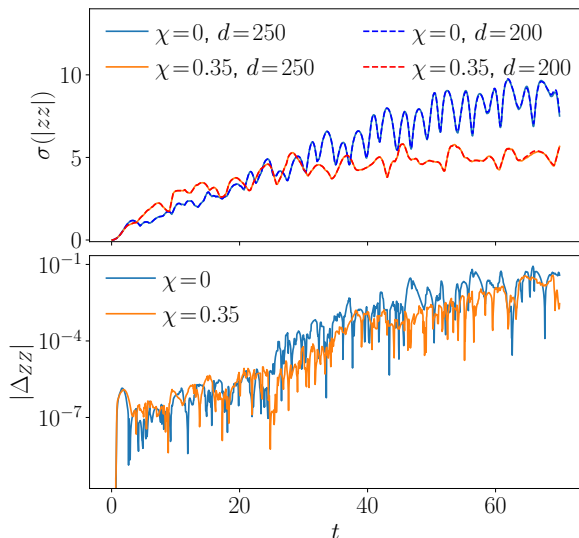


FIG. S3. (Color online). Root mean square of the spread of the connected correlator between Pauli Z matrices at the middle site and other sites in the chains for various values of χ for two different bond dimension. The bottom panel shows the absolute value of the difference of that quantity between $d_{\max} = 250$ and $d_{\max} = 200$.

approximation [S5]. It allows to compute a better approximation of the scarred states and also includes other eigenstates. As was the case for the FSA, the basis states on which this approximation is built are independent of χ , and the confining term is perfectly captured for all values.

Probing fidelity after quenches from the Néel state leads to unusual results (see Fig. S5). The non-monotonic behaviour is still there, but now the system size scaling is non-trivial. For generic values of χ , the fidelity decays as L_m increases. The only values of χ for which this does not happen are $\chi = 0$, $\chi = \infty$ and $\chi = 0.41$, hinting that these are all special points. This is expected for $\chi = 0$ and $\chi = \infty$, as in these two cases one of the two terms in the Hamiltonian is completely removed. However it is quite a strong result for $\chi = 0.41$ as it implies that the fidelity improvement is not a mere finite-size effect but a more fundamental change.

For an infinite-system, the dynamics in the symmetric subspace admits a classical description using the time-dependent variational principle (TDVP) Ansatz [S5–S7]. The quantum state is parametrized using two θ angles that relates to the excitation density on each sublattice (θ_o and θ_e) and two ϕ angles that describe phases (ϕ_o and ϕ_e). This corresponds to two spin-coherent states (one on each sublattice), on which a projector was applied to eliminate all states that violate the PXP constraint. This Ansatz was developed to give a semi-classical limit for the Néel state revivals at $\chi = \mu = 0$, but it also holds for $\chi \neq 0$. The equations of motion are the same as in Eqs. (9a) and (9b) of Ref. [S7] for $C = 2$, except that now for $\mu_z = +\chi$ for ϕ_1 and $\mu_z = -\chi$ for ϕ_2 . We

integrate numerically the equations of motion starting from the Néel state, and compute the excitation density on each sublattice from them. Fig. S6 shows the results for TDVP and for ED in system with $L_m = 20$. The TDVP Ansatz used simulates a system of infinite size, so we do not expect both sets of results to match at longer times where finite-size effects will occur for the ED data. Nonetheless, we see a good agreement at shorter times, and that for all values of χ .

Nonetheless, there is a major difference between the cases $\chi = 0$ and $\chi \neq 0$. For the former, the two ϕ angles are dynamically frozen when starting from the Néel state and there are only two independent degrees of freedom. As a consequence chaos cannot develop and every trajectory is either periodic (like the Néel and anti-Néel one) or it goes asymptotically towards a fixed point. For $\chi \neq 0$, the ϕ angles are no longer frozen and the system has 3 independent degrees of freedom (4 angles, but energy conservation means that they are not all independent) and chaos can develop. We find that for $\chi \neq 0$ the trajectory is no longer exactly periodic, highlighting the instability of the Néel periodic orbit at $\chi = 0$. Despite this, we still find that monitoring the excitation density will show persistent oscillations. The expectation of $\langle \hat{n}_o \rangle$ after one period (meaning at its first local maximum) shows the same non-monotonic behaviour as in the quantum system, at least qualitatively, as shown on Fig. S7.

In order to have a better understanding of the dynamics between revivals, we can plot the expectation values of $\langle \hat{n}_o \rangle$ and $\langle \hat{n}_e \rangle$ against each other over time. This is plotted in the two bottom panels of Fig. S7 using data from both ED and TDVP. As expected, both sets of results give similar results. The TDVP data shows better revivals in the sense that successive “loops” with the same χ are almost on top of each other, so the orbit is close to periodic.

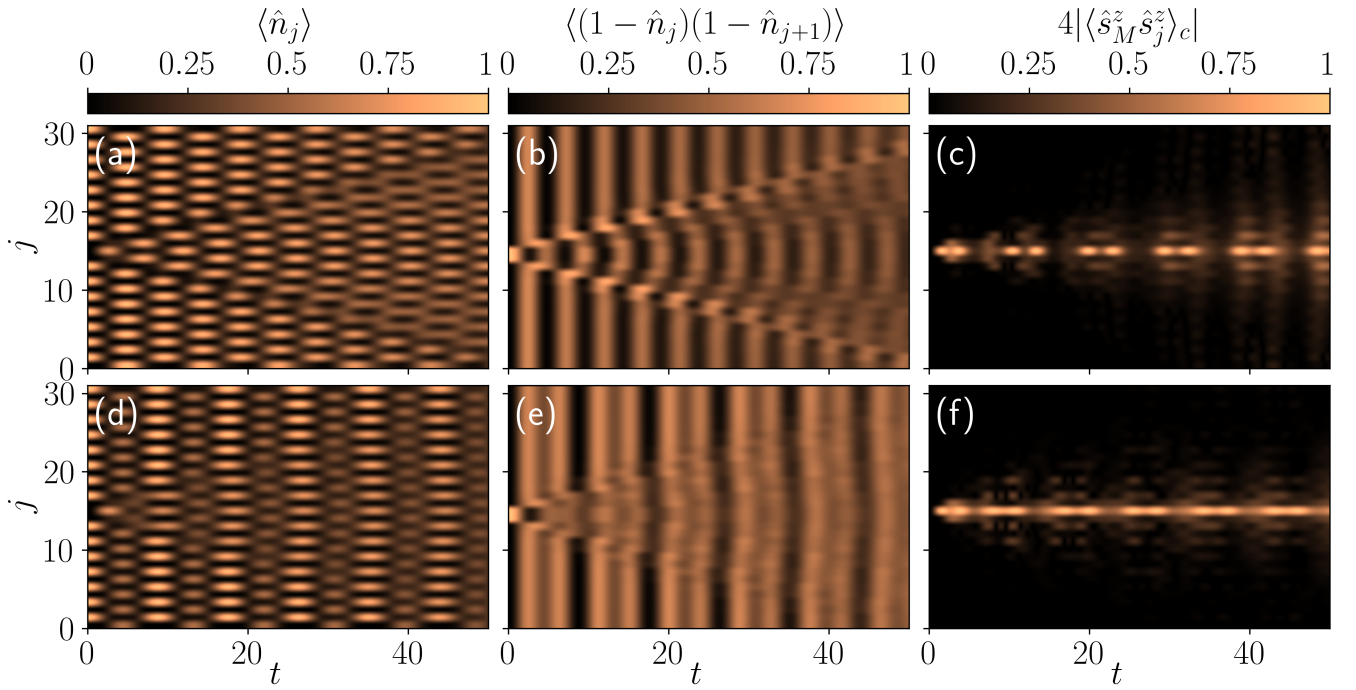


FIG. S4. (Color online). Observables dynamics after a quench from the Néel states with a defect with $L_m = 32$. (a)-(c) $\chi = 0$ (d)-(f) $\chi = 0.35$. The effect of confinement is visible for the ZZ correlator in panels (c) and (f). At late times, the Néel and anti-Néel domains are still clearly distinguishable in panels (a) and (b) but not in panels (c) and (d).

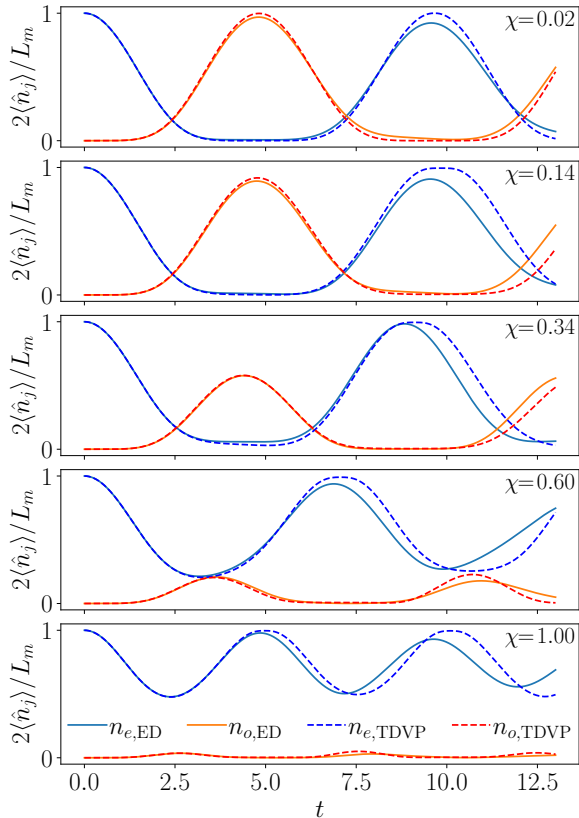


FIG. S6. (Color online). Sublattice occupation after a quench from the Néel state as obtained with ED and $L_m = 20$ and with TDVP. The data agrees well up to the first revival for all values of χ .

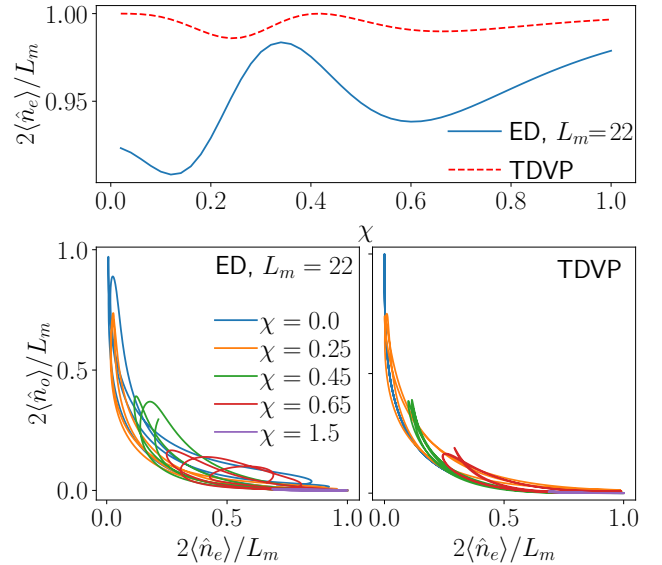


FIG. S7. (Color online). Comparison between TDVP and ED data for sublattice excitation density. Top: value of the even sublattice excitation density after one period. The same qualitative behaviour can be seen in ED and TDVP data. Bottom: trajectory of the two sublattice excitation densities. The TDVP data shows trajectories that are closer to periodic.

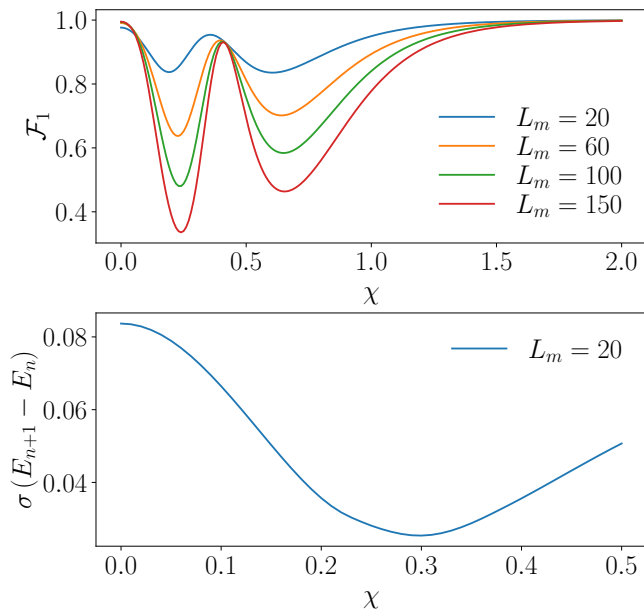


FIG. S5. (Color online). Results for confined scarring in the symmetric subspace approximation. Top: Revival fidelity from the Néel state for various system sizes. Bottom: Standard deviation of the energy spacings of the scarred eigenstates. Both the best revival fidelity and the most equal energy spacing show optimal points between 0.3 and 0.5. The only values of χ for which the fidelity does not decay with system size are $\chi = 0, \chi = \infty$ and $\chi = 0.41$.

[S1] S. Bravyi, D. P. DiVincenzo, and D. Loss, *Annals of Physics* **326**, 2793 (2011).
[S2] I.-C. Chen and T. Iadecola, *Phys. Rev. B* **103**, 214304 (2021).
[S3] P. Fendley, B. Nienhuis, and K. Schoutens, *Journal of Physics A: Mathematical and General* **36**, 12399 (2003).
[S4] J. Hauschild and F. Pollmann, *SciPost Phys. Lect. Notes*, 5 (2018), code available from <https://github.com/>

[tenpy/tenpy](https://github.com/tenpy/tenpy).
[S5] C. J. Turner, J.-Y. Desaulles, K. Bull, and Z. Papić, *Phys. Rev. X* **11**, 021021 (2021).
[S6] W. W. Ho, S. Choi, H. Pichler, and M. D. Lukin, *Phys. Rev. Lett.* **122**, 040603 (2019).
[S7] A. A. Michailidis, C. J. Turner, Z. Papić, D. A. Abanin, and M. Serbyn, *Phys. Rev. X* **10**, 011055 (2020).